Ultraviolet Sizes and Morphology of Galaxies in the Coma Cluster

by

Cameron Morgan

A thesis
presented to the University of Waterloo
in fulfillment of the
thesis requirement for the degree of
Master of Science
in
Physics

Waterloo, Ontario, Canada, 2022

© Cameron Morgan 2022

Author's Declaration

This thesis consists of material all of which I authored or co-authored: see Statement of Contributions included in the thesis. This is a true copy of the thesis, including any required final revisions, as accepted by my examiners.

I understand that my thesis may be made electronically available to the public.

Statement of Contributions

The research comprising this thesis was conducted under the supervision and advice of Michael Balogh. The data analyzed for this project comes from two proposals (PIs Michael Balogh and Pat Côté) that were awarded time on the Ultraviolet Imaging Telescope. The raw data was processed by the Indian Space Research Organization and Joe Postma. I would like to acknowledge and thank Mike Hudson for providing the HECTOSPEC catalogue of spectroscopic redshifts (PI Ron Marzke) used in this analysis, and also Louise Edwards for providing catalogues of infrared data of the Coma cluster (not used in the analysis presented herein).

Figure 1.1 was pulled from Springel et al. (2005b), Figure 1.2 from Driver et al. (2022), Figure 1.3 from Cramer et al. (2019), Figure 4.7 from Yagi et al. (2010), Figure 5.1 from Cortese et al. (2012) and Figure 5.5 from Moran et al. (2006).

All other work in this thesis is my own.

Abstract

We present a study of the Coma cluster using ultraviolet (UV) imaging obtained using the Ultraviolet Imaging Telescope. We discuss methods for measuring sizes and morphology of galaxies in the UV. Several cluster galaxies in our sample exhibit small UV sizes relative to their optical sizes, while we find that galaxies in a field sample have similar sizes in UV and optical bands. Further, we have shown that when cluster and field galaxies are matched up one-to-one based on colour and absolute i-band magnitude, the cluster galaxies tend to have smaller UV sizes than their field counterparts. We have used an $NUV - i$ colour magnitude relation to identify a red sequence and blue cloud of galaxies in our sample. There is a trend whereby redder disk galaxies exhibit even smaller UV sizes, relative to field counterparts, than galaxies at the bluer end of the spectrum. Since this result is consistent with environmentally driven gas stripping, we have identified from our sample six known stripping candidates, and further identified one new candidate. Additionally, we find that this sample of galaxies exhibits redder UV-optical colours in the outer regions of the galaxy, a result consistent with an outside-in quenching mechanism affecting the galaxy. Beyond the blue cloud, we find a substantial population of red disks/spirals in our sample; as high as 38% of galaxies using an $NUV - i = 4.0$ cut to separate blue and red galaxies. This result is highly dependent on the definition of the red sequence, however. The existence of red spirals has been discussed in the literature as a possible indication of starvation lowering the rates of star formation in previously blue spirals while not disturbing the overall morphological structure of the galaxy. We have discussed these results in context as potential indicators of various environmentally driven quenching mechanisms underway in the Coma cluster, and discussed future surveys that will allow a more robust quantification of the prevalence of these mechanisms.

Acknowledgements

I would like to begin by thanking Dr. Michael Balogh. This project presented many challenges, and its completion would not have been possible without your advice and expertise. I feel privileged to be working with such a supportive and encouraging supervisor, and I am looking forward to the projects we have lined up for the future.

Additionally I would like to thank my parents and my sister for their support, for checking in on me and always lending an ear. I would like to extend this thanks to Daniel and Karyn; since the beginning of undergrad your friendship has supported me more than you probably know.

Finally I would like to thank Cait, for supporting and encouraging me and for keeping me grounded, for the adventures that allowed me to take mental breaks from work, for being my fishing buddy, and for keeping me company in the office on a Sunday when I was in the throes of writing this thing.

Dedication

For Grandpa: thanks for all you did and all you were. I'll miss you.

Randy Burgess - May 24th, 1949 - August 4th, 2022

Table of Contents

List of Figures

x

List of Tables

Chapter 1

Introduction

The currently-accepted model that describes the structure of the universe is the ΛCDM model. In this model, the universe is dominated by a cosmological constant known as dark energy (Λ), a form of energy first proposed by Albert Einstein to explain a static universe and later adopted to explain observations of an accelerating universe (Einstein 1917; Riess et al. 1998; Perlmutter et al. 1999). The remainder of the universe is comprised of matter and radiation, the majority of which is thought to be cold dark matter (CDM). Evidence for dark matter was originally found by Zwicky (1933) which he used to explain the rotation curves observed in the Coma cluster for which the luminous matter appeared to be insufficient. Cold dark matter theory, first proposed by Peebles (1982) and further developed by Blumenthal et al. (1984), incorporates hierarchical structure growth of the universe. In this model, quantum fluctuations in the very early universe led to overdense regions in space after a period of rapid cosmic inflation. These slight overdensities can be observed in the structure of the cosmic microwave background (CMB): the leftover photons set free once the universe had cooled enough to form neutral atoms at about 380,000 years after the Big Bang. The Planck mission set out to measure the anisotropies in the CMB at extremely high resolution, and with the final data release in 2018 showed that the universe is made up of 68.5% dark energy and 31.5% matter (26.4% dark matter and 5.1% baryonic matter) and is flat (Planck Collaboration et al. 2020). Over time, the relic overdensities observed in the CMB accreted matter gravitationally, beginning with dark matter due to the fact that it does not react with light and as such cannot feel radiation pressure. The mass function of dark matter halos has been determined through many theoretical models and simulation studies, beginning with Press & Schechter (1974). The work of Sheth et al. (2001) extended the Press-Schechter model beyond the assumptions of spherical collapse and Gaussianity in the initial density fluctuations. A wealth of simulation studies have

modelled the halo mass function and its redshift evolution (e.g. Jenkins et al. 2001; Reed et al. 2003; Springel et al. 2005b; Reed et al. 2007; Watson et al. 2013). We show in Figure 1.1 the redshift evolution since $z \sim 10$ of the halo mass function from Springel et al. (2005b). This figure shows the hierarchical build up of halos over time, with recent epochs hosting higher numbers of massive halos. Additionally, measurements of galaxy cluster and group abundances have shown good agreement with predictions of CDM models (e.g. Bahcall & Cen 1993; Reiprich & Böhringer 2002; Böhringer et al. 2017; Driver et al. 2022). The most recent work by Driver et al. (2022) measured the halo mass function using the Galaxy And Mass Assembly (GAMA) combined with Sloan Digital Sky Survey (SDSS) and the ROSAT-ESO Flux Limited X-ray Galaxy Cluster Survey (REFLEX-II) data and found good agreement with ΛCDM predictions, as shown in Figure 1.2.
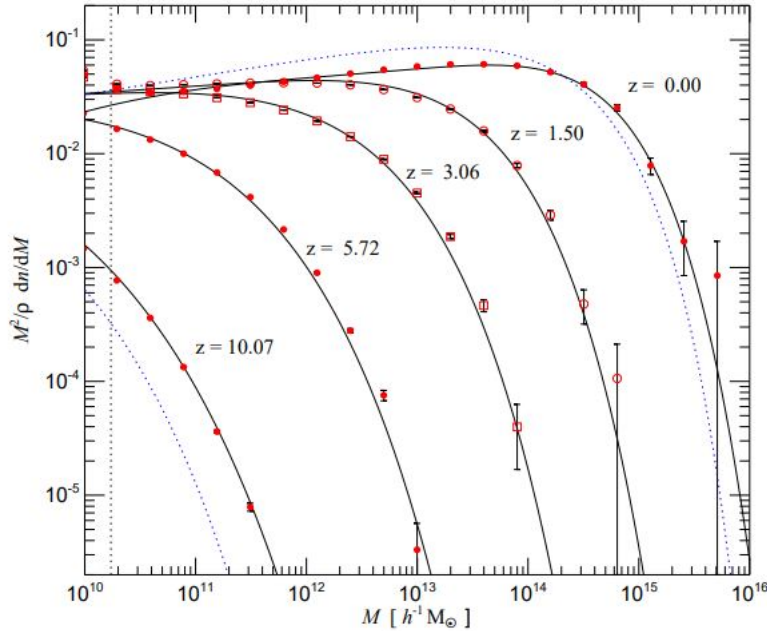
Figure 1.1: Figure 2 from Springel et al. (2005b), showing the redshift evolution of the differential halo mass function using the Millennium Simulation.
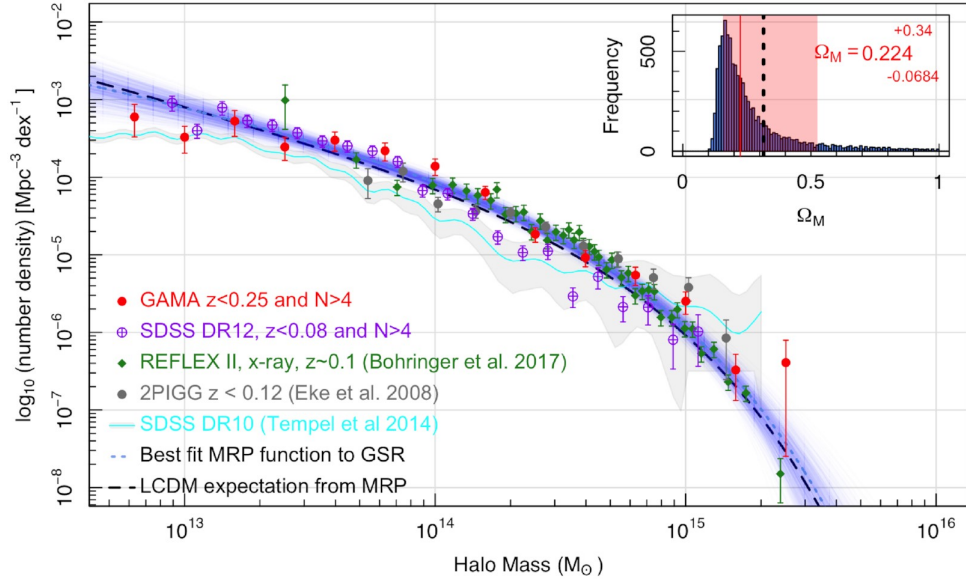
Figure 1.2: Figure 11 from Driver et al. (2022) showing their empirical halo mass function compared to ΛCDM predictions.

It is within dark matter halos that galaxies can form through the cooling and condensing of gas to form stars in a galactic disk. The observed redshift evolution of the galaxy stellar mass function (GSMF) shows that more massive galaxies existed earlier, with less massive galaxies slowly building up their mass over time (e.g. Pozzetti et al. 2003; Fontana et al. 2004; Drory et al. 2005; Bundy et al. 2005; Muzzin et al. 2013; Behroozi et al. 2013). Additionally, earlier models of radiative gas cooling showed that, in the absence of any energy input, the cooling of gas would be too efficient (Cole 1991; White & Frenk 1991). These discoveries became proof that galaxy evolution and the evolution of the stellar mass function does not simply follow the evolution of dark matter halos (Bower et al. 2006). More recently, several sources of feedback have been incorporated into models to prevent overly-efficient gas cooling. One such feedback mechanism has been dubbed *squelching*, and affects low mass halos that have virial temperatures approximately equal to the ionization temperature of hydrogen, $\sim 10^4$K (Somerville 2002; Somerville & Davé 2015). Another form of feedback that dominates star formation suppression in low-mass galaxies is stellar wind, whether it be from massive stars or supernovae (see Veilleux et al. 2005; Somerville & Davé 2015 for discussion, and Efstathiou 2000; Hopkins et al. 2012, 2014 for examples of simulations). The dominating feedback suppressing star formation in more massive galaxies is feedback from active galactic nuclei (AGN), which can heat and ionize gas, as well as mechanically eject it from the galactic disk (Springel et al. 2005a; Di Matteo et al.

2005; Somerville & Davé 2015). As such, the formation and continued evolution of galaxies is determined by the ongoing exchange of baryonic material with the surrounding universe through internal and external mechanisms.

As hierarchical structure growth continues, systems of galaxies in halos merge together and form larger structures such as galaxy clusters. These galaxy clusters have grown to become amalgamations of hundreds or thousands of galaxies bound together in a combined potential well. Gas accreted into the dense environment of the cluster becomes superheated to form the intra-cluster medium (ICM), which emits at x-ray wavelengths via the process of *Bremsstrahlung* radiation. The heating of the ICM is primarily driven through gravitational heating (Kaiser 1986), but other mechanisms, including feedback, may also be important for temperature regulation (Quilis et al. 2001; Tornatore et al. 2003; Yang & Reynolds 2016). Additionally, the high temperatures of the ICM allow emission line radiation from even heavy elements to be observed.

Galaxies in the local universe exist in a bimodality of colours and star formation rate (SFR). On one end, "late-type galaxies" are often characterized by disks and spiral arms, are blue in colour and teeming with star formation activity. Opposingly, "early-type galaxies" are typically red in colour, ellipsoidal in shape, and lack ongoing star formation. Massive galaxies are more likely to be quiescent (Muzzin et al. 2013; Balogh et al. 2016), and measurements of the SMF at different redshifts show a build-up in the quiescent population (Faber et al. 2007). This implies that star-forming galaxies undergo quenching to transition to the passive population. It has been known for some time that galaxy clusters have a higher proportion of early-type galaxies than what is found in the field (Dressler 1980b; Butcher & Oemler 1984). This morphology density relation has been well studied in the local universe, for example using the Sloan Digital Sky Survey (SDSS; Goto et al. 2003b). Alongside the morphology density relation, cluster galaxies have been shown to exhibit lower SFR than those in the field, especially at low redshift (Balogh et al. 1997, 1998; Lewis et al. 2002; Gómez et al. 2003; Wetzel et al. 2012; Kauffmann et al. 2004; Baldry et al. 2006; Weinmann et al. 2006). More recent work by Sazonova et al. (2020a) extended the study of the morphology-density relation to galaxy clusters in the redshift range $1 < z < 2$, determining that the drivers of this relation were in place at earlier redshifts. Cluster galaxies have also been shown to have a deficiency of molecular gas at fixed stellar mass as compared to field galaxies in the local universe (Giovanelli & Haynes 1985; Cortese et al. 2011; Boselli et al. 2014), and recently in the $1 < z < 2$ redshift range (Alberts et al. 2022). Using the FourStar Galaxy Evolution (ZFOURGE) survey, Kawin-wanichakij et al. (2017) quantified the redshift evolution of the environmental quenching efficiency in different stellar mass bins. Their work shows that at $z > 0.5$, the environmental quenching efficiency depends strongly on stellar mass, with the population of low-mass,

4

quenched galaxies building up over time more quickly than that of high mass galaxies. These results show that environmental quenching in dense environments is the key driver for quenching of low-mass galaxies, and are consistent with environmental quenching efficiencies measured from other surveys that targeted smaller ranges of redshift and stellar mass (SDSS, zCOSMOS; Peng et al. 2010b, SpARCS; Nantais et al. 2016). It has become quite evident that galaxies in dense environments evolve differently from those in the field, and an ongoing field of interest is improving theoretical models of galaxy evolution to produce the observed environmental trends (Weinmann et al. 2012; De Lucia et al. 2012).

Environmental effects in galaxy clusters that negatively impact star formation can be classified into three categories. First, there are processes that act to remove gas from the galactic disk. This includes ram-pressure stripping (RPS), which occurs as orbiting galaxies interact with the ICM. The pressure exerted is proportional to ρv^2, where ρ is the density of the ICM and v is the velocity of the galaxy relative to the ICM (Gunn & Gott 1972). Of course, the gas in the galactic disk is bound to the gravitational well of the galaxy, so in order to strip gas from the disk, the pull of the ICM must exceed the restoring force of the disk, which exerts a force per unit area of $2\pi G \sigma_s \sigma_g$, where σ_s and σ_g are the surface mass densities of stellar and gaseous material respectively. If the force of the ram pressure can overcome the restoring force, gas is stripped from the galactic disk, resulting in a tail of material that can be observed extending beyond the plane of the galaxy along the vector that describes the motion of the galaxy. As such, ram pressure stripping is more likely to affect smaller galaxies with lower restoring force. RPS is, in its simplest form, an outside-in quenching mechanism; the dynamics of the stripping event will pull gas away from the outer regions of the galactic disk first, shutting down the star formation in the outer regions of the galaxy. However, simulations of ram-pressure stripping have shown that the effectiveness of the mechanism depends on the distribution of gas in the galactic disk, as well as the inclination angle of the galaxy and the nature of the central potential (Abadi et al. 1999; Quilis et al. 2000; Marcolini et al. 2003; McCarthy et al. 2008; Tonnesen & Bryan 2009). A comprehensive study simulating the evolution of gas in the disks of galaxies in the Virgo cluster showed results consistent with HI 21cm observations (Vollmer et al. 2001). The close proximity of Virgo makes it possible to measure spatially resolved velocity fields of HI and molecular gas. These results showed that the efficacy of ram-pressure stripping is sensitive to the orbital parameters of the galaxy. Galaxies undergoing ram-pressure stripping were sometimes able to re-accrete stripped gas back onto their disks. This re-accretion was more effective for galaxies being stripped edge-on, i.e. having low inclination angles Vollmer et al. (2001). GAs Stripping Phenomena in galaxies with MUSE (GASP) is a recent project undertaken to study gas stripping processes using spatially resolved spectroscopy of extreme examples of galaxies undergoing gas stripping,

known as "jellyfish galaxies" (Poggianti et al. 2017). When looking at a sample of jellyfish galaxies in projected phase space, Jaffé et al. (2018) found that the peculiar velocities of RPS candidates are higher than those of the underlying cluster population. They also note that galaxies with the most extreme tails of stripped gas are preferentially located near the centre of the cluster and are moving at high-speed relative to the cluster. These findings suggest that galaxies experiencing RPS are typically on their first infall into the cluster on radial orbits. The discovery that the stripped tails were most extreme at high velocity and near the centre of the cluster builds the case further for RPS since the ICM density is higher near the cluster centre, and as such galaxies moving rapidly near the centre would experience the greatest RPS force. Another effect of RPS is its supposed ability to initially induce star formation in the disk of a galaxy by compressing the interstellar medium. The GASP project showed that in their sample of galaxies, the RPS candidates did in fact show heightened rates of star formation relative to galaxies that were not being stripped (Vulcani et al. 2018). They also noted that star formation also occurs in the tail of stripped gas. This is consistent with predictions of a ram-pressure induced burst of star formation in the early stages of the stripping process prior to quenching (see for example, simulation studies by Steinhauser et al. 2012; Bekki 2014). Complimentary results were obtained by Roberts & Parker (2020) in a sample of optically-identified stripping candidates in the Coma cluster, as well as by Roberts et al. (2022a) when looking at over 50 groups and clusters using deep optical imaging from the Canada France Hawaii Telescope (CFHT) as part of the Ultraviolet Near-Infrared Optical Northern Survey (UNIONS). The enhanced star formation due to compression of the ISM would be expected on the leading edge of the galaxy as it pushes through the ICM. Looking at the Perseus cluster, Roberts et al. (2022b) found four stripping candidates that all showed enhanced star formation on the leading edge through multi-wavelength imaging and the spatial distribution of Hα sources in the galaxy.

Galaxies in clusters experience gravitational effects due to their position in the cluster. Tidal forces are caused by gravitational interactions with the central potential of the cluster. Galaxies may also experience mergers and close encounters with other galaxies. These interactions can cause gas on the galactic disk to lose angular momentum and fall to the centre of the cluster, thereby inducing a rapid burst of star formation (Moore et al. 1996). This burst can rapidly consume the remaining cold gas in the disk of the galaxy that is necessary to continue forming stars. While tidal stripping can also pull gas away from the galactic disk, it can be distinguished from ram-pressure stripping. Tidal forces act to create curved tails on both the near and far side of the galaxy along the vector of the tidal force. Additionally, while ram-pressure stripping affects only gas, tidal stripping can also pull stars from their orbits around a galaxy. Thus, one way to distinguish tidal stripping

from RPS is to look for older stellar populations in the stripped material.

Finally, star formation can be shut down indirectly through processes such as starvation or strangulation, whereby fresh supplies of gas accrete onto the central potential of the cluster instead of onto individual galaxies. This process cuts off the supply of fresh gas needed for a galaxy to continue forming stars, leaving the galaxy quiescent once it has consumed all the gas in its disk. Starvation is a passive quenching process, and would be expected to not greatly disturb the morphology of a galaxy the way gas stripping does. Additionally, while RPS acts quickly to quench star formation, starvation would be a much slower process, as the galaxy gradually uses up its stores of gas over gigayears. van den Bosch et al. (2008) studied central-satellite pairs of galaxies to investigate the drivers of satellite quenching. They determined that the mechanisms most responsible for satellite galaxy quenching had more of an affect on the colour of the galaxy than on its morphology, and that there was no dependence on halo mass of the differences in colour and morphology for matched central satellite pairs. These results are more consistent with starvation being the dominant mechanism for the slow quenching of satellite galaxies. Considering processes like starvation as being key elements in the overall quenching of galaxies is important especially when considering the outer regions of clusters, or smaller galaxy groups, where the ICM density is much lower and ram-pressure stripping may not be as effective. Recent work by Kolcu et al. (2022), however, has identified ram-pressure stripping candidates in galaxy groups, that fit the morphological definitions outlined by previous studies of stripping candidates in clusters. Once again, this highlights the importance of a consideration of different quenching mechanisms to paint a grand picture of environmental effects in dense environments. Determining robustly trends in which mechanisms dominate is an area of ongoing research.

The Coma cluster is the closest massive galaxy cluster, containing over 1000 confirmed member galaxies and located at a distance of ~ 100kpc. The Virgo cluster is smaller than Coma by a factor of about 10, but is much closer. As such, Virgo can be studied with higher spatial resolution than Coma, but Coma may have more extreme environmental effects due to its larger size. Smith et al. (2010) used ultraviolet (UV) imaging from the Galaxy Evolution Explorer (GALEX; Martin et al. 2005) to pinpoint 13 gas stripping candidates by identifying tails of stripped gas oriented predominantly away from the cluster centre. Additionally, they found a higher proportion of blue galaxies undergoing stripping events closer to the centre of the cluster, suggesting these galaxies are typically on their first infall through the ICM. Yagi et al. (2010) drew similar conclusions when identifying 14 extended Hα clouds around Coma cluster galaxies, connecting their results with those of Smith et al. (2010). Most recently, Roberts & Parker (2020) used optical imaging from CFHT to identify potential disturbed morphologies in Coma member galaxies and

identified trends in measurements of morphological parameters. A fascinating example of likely ram-pressure stripping in the Coma cluster is GMP 2910, also known as D100. The tail of Hα emission seen in Figure 1.3 is 60 kpc long, first identified by Yagi et al. (2007).

Figure 1.3: Galaxy D100 (GMP 2910), from Cramer et al. (2019). The bright red tail is Hα imaging from Subaru Suprime-Cam by Yagi et al. (2007).

Ultraviolet (UV) emission is emitted by young, hot stellar populations, making it a powerful tracer of recent and ongoing star formation on the order of 100 million years. In addition to dominating the emission of O and B-type stars, UV light emanates from stars on the hot horizontal branch, and is also produced from active galactic nuclei (AGN). A mystery in the evolution of early-type galaxies is known as the UV-upturn: some early-type galaxies show increasing flux with decreasing wavelength at $\lambda \sim 2000$ Å in the UV regime (Aaronson et al. 1978; Greggio & Renzini 1990; Dorman et al. 1995). This excess UV emission is not predicted by standard spectral energy distribution (SED) modelling, and while theories into its origins exist, a robust model of the UV-upturn remains largely undiscovered. Studying the morphology of galaxies at UV wavelengths can provide information about their recent star formation, and give clues into processes that may be quenching star formation in the galaxy. Specifically, comparing galaxies in clusters and the field using UV imaging can provide insight into which environmental effects are at play in clusters and

the relative strength of these effects. When looking at galaxies in the Herschel Reference Survey (HRS; Boselli et al. 2010), Cortese et al. (2012) compared the structural scaling relations of Hɪ-deficient galaxies in the sample to Hɪ-normal galaxies, finding smaller UV sizes in the Hɪ-deficient sample. They further connect this trend to gas removal of the portion of the HRS sample that are members of the Virgo cluster. Cortese et al. (2012) also showed that Hɪ-deficient galaxies showed substantially redder colours in the outer regions of the galaxies as compared to HI-normal galaxies, while the inner regions were less affected. This evaluation of UV-optical colour gradients across the planes of galaxies leads to the inference that an outside-in quenching mechanism such as ram-pressure stripping is working to quench galaxies in dense environments. The use of GALEX UV imaging is also what allowed Smith et al. (2010) to identify ram-pressure candidates in Coma. Since UV emission traces recent star formation, its signature from stripped gas indicate ongoing star formation is the stripped material.

In this work we study a sample of Coma cluster galaxies using high-resolution ultraviolet imaging. We measure the sizes of galaxies using three different methods and compare to the underlying optical sizes. Further, we compare trends in the UV sizes of the cluster sample to a sample of field galaxies, along the way identifying examples of cluster effects impacting the evolution of member galaxies. This work builds upon previous studies that have looked into environmental effects in the Coma cluster (Smith et al. 2010; Yagi et al. 2010; Roberts & Parker 2020), but at a higher resolution than previous UV studies. Our results are consistent with results in the literature that indicate the presence of both outside-in quenching mechanisms at play in clusters, and also passive quenching of star formation that produces red spiral galaxies.

The remainder of this thesis is structured as follows: in chapter 2 we present the UVIT data used in this report, discuss source extraction and supplementary data. Chapter 3 highlights the methods we use to measure UV sizes of galaxies. In chapter 4 we present the results of measuring galaxy sizes and looking at the morphology of sample galaxies. Chapter 5 involves a discussion comparing our results to the literature, and discussing future work. We present conclusions in chapter 6.

Chapter 2

Data

2.1 Imaging Coma with the Ultraviolet Imaging Telescope

The data used in this study comes from two proposals that were awarded time on the Ultraviolet Imaging Telescope (UVIT) on ASTROSAT to image the Coma cluster (Abell 1656) in ten regions covering about 2 sq. deg of the cluster out to the virial radius at 1.1deg (1.9Mpc) (PIs Côté and Balogh). The motivation for these proposals stems from studies of the Coma cluster using the Galaxy Evolution Explorer (GALEX; Martin et al. 2005). These studies (e.g. Cortese et al. 2008; Smith et al. 2010; Hammer et al. 2012) mapped the UV luminosity functions of Coma and identified candidates of gas stripping. Imaging from GALEX, however, was only possible in two broadband UV channels, which made it difficult to differentiate between possible explanations for the UV-upturn observed in some galaxies. Additionally, while the $\sim 5''$ resolution of GALEX was sufficient for Smith et al. (2010) to identify stripping candidates, greater resolution would be needed for a more detailed study of UV morphology of Coma galaxies. As the successor to GALEX, UVIT allows imaging in several narrowband UV filters in both the far-UV (FUV) and near-UV (NUV), and has a nominal resolution of $1.8''$. The actual resolution of UVIT imaging reaches $\sim 1.2''$, which at the distance of the Coma cluster corresponds to 0.58kpc, much smaller than a typical galaxy scale length (Tandon et al. 2020). The pixel scale of the data is 0.417arcsec/pixel.

The data used in this research was received from the Indian Space Research Organization and processed by Joe Postma using CCDLAB (Postma & Leahy 2017). CCDLAB is

a data reduction pipeline used for processing UVIT data for scientific use. The pipeline involves steps such as drift correction and creation of an exposure time array from each frame in a given observation (see Postma & Leahy 2017 for a full review of the pipeline).

For this project, data from only two regions was available for analysis, as outlined in Table 2.1. 5σ detection limits are calculated using SExtractor flux measurements to determine where the total signal-to-noise of the galaxy exceeds 5. The noise in these calculations is made up of the source noise as well as the background noise in an elliptical aperture outlining the object. While the majority of the work in this thesis will focus on broadband NUV imaging, the initial source extraction step is performed on each available filtered image, as outlined in Table 2.2.

Table 2.1: Coma cluster regions

Region	RA (deg)	DEC (deg)	Distance from cluster centre	NUVF1 exposure time (s)	5σ magnitude limit
Coma5	195.1269	27.7696	$0.23R_{200}$	1867.7	$m_{NUV} = 24.44$
Coma7	195.5321	28.2742	$0.50R_{200}$	2029.8	$m_{NUV} = 24.53$
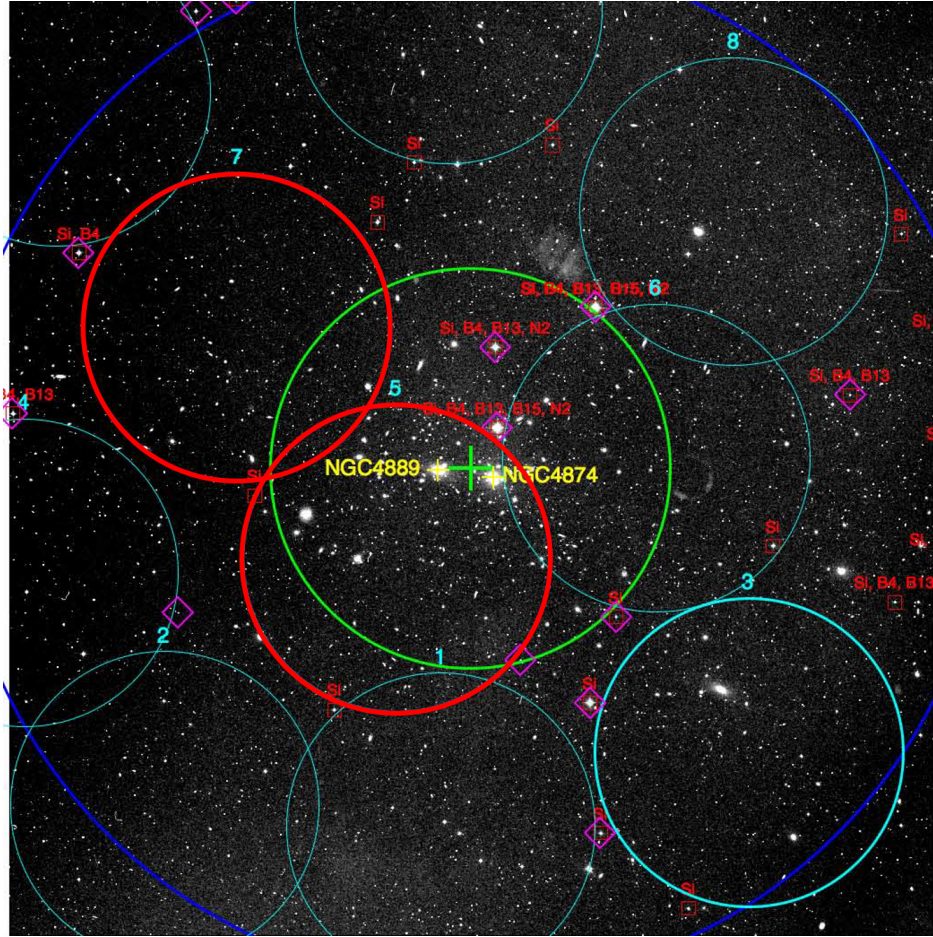
Figure 2.1: Figure from UVIT Coma proposal (P.I. Balogh) showing ten proposed regions in Coma in cyan and red, where red are the regions with data in this thesis, referred to as "Coma5" and "Coma7". The large blue circle outlines the virial radius of the cluster at 1.1 deg.

2.2 Source Extraction and Ancillary Data Matching

2.2.1 Background Subtraction Routine

We perform source extraction using SExtractor (Bertin & Arnouts 1996) on all four UV images from each of the two regions to create a catalogue of UV sources. Owing to the

Table 2.2: Filters used in UVIT imaging of the Coma cluster

| Filter | λ_{eff} | $\Delta\lambda$ |
	Å	Å
NUVF1	2418	785
NUVF3	2447	280
NUVF5	2632	275
FUVF2	1541	380

faintness of the sky background at UV wavelengths, the internal background estimators within SEXTRACTOR failed to accurately determine local or global background measurements on UVIT images. Instead, we follow closely the work of Morrissey et al. (2007) to measure the background outside of SEXTRACTOR. First, a rough global background value is determined by manually selecting several regions away from bright sources in the image, and recording the mean pixel value. This initial global estimate of the background is then subtracted off the original image and the image is run through SEXTRACTOR with its background estimation turned off. The sole purpose of this initial SEXTRACTOR run is to produce a segmentation map of the bright sources in the image so that the background can be measured more locally. From here, we use the segmentation map produced in the initial SEXTRACTOR run to mask bright sources in the original science image, and divide the image into bins of 256×256 pixels ($106 \times 106''$). In each bin we compute the mean pixel value (with bright sources masked) and fit a Poisson distribution $P_k(x)$ where $P_k(x)$ is the likelihood of observing k events given a mean number of events x. From here, as in Morrissey et al. (2007), we iteratively clip any pixels with values of k where $P_k(x) < 1.35 \times 10^{-3}$, which corresponds to 3σ in a Gaussian distribution. Once no more pixels need to be clipped, the resulting mean is the background value in the given bin. Once a background map is completed with local values in each bin, this background map is subtracted from the original images to create a background subtracted image. This background subtraction routine is performed on each image in the four filters, as well as a stacked image created simply by adding the arrays of the four images together to create a detection image with higher signal-to-noise.

Once background subtraction is complete, we run SEXTRACTOR again, this time with the goal of creating a catalogue of UV sources. This run of SEXTRACTOR uses double-image mode where the first image is used solely for detection and the second image for photometric measurements (Bertin & Arnouts 1996). The stacked, background subtracted image is used as the detection image, and then each filtered, background subtracted image is used in turn to make photometric measurements in each of the four filters. The resulting

catalogue contains thousands of detections comprising stars, galaxies in the Coma cluster, and background galaxies with photometric measurements in the four UV filters.
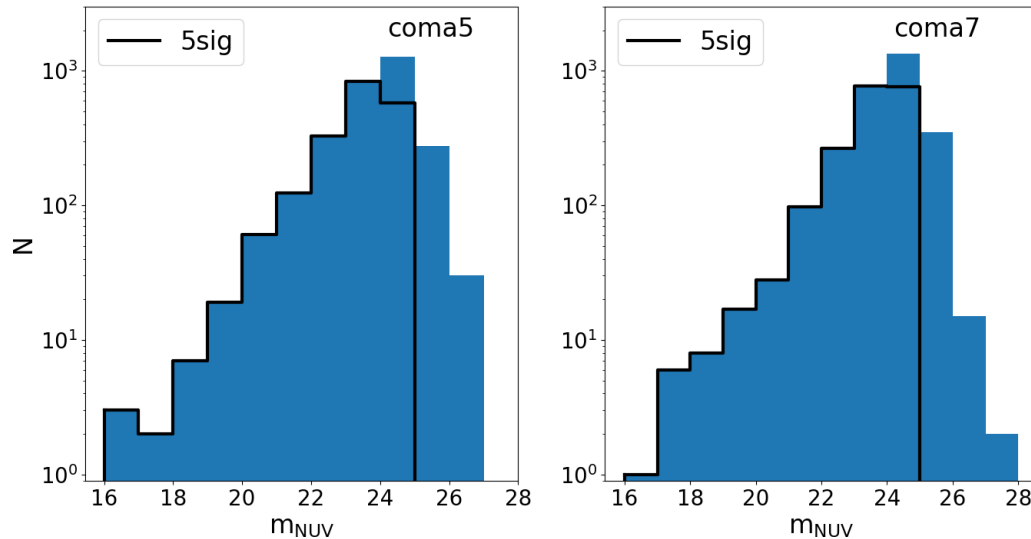
Figure 2.2: SEXTRACTOR detections in each Coma region. The solid black line highlights the distribution of galaxies with S/N > 5.

In order to obtain optical photometry and spectroscopy for our sample of UV detections, we initially turned to the Sloan Digital Sky Survey (SDSS; York et al. 2000; Ahumada et al. 2020). The SDSS pipeline, however, has a tendency to over-deblend large, bright galaxies, producing unreliable photometric measurements. To circumvent this issue, we supplement with the NASA-Sloan Atlas (NSA; Blanton et al. 2011). The NSA was a project undertaken with the purpose of developing a pipeline that would produce more reliable photometric measurements for galaxies in the local universe than SDSS. Because of this, we elect to always match our detections to the NSA first, and SDSS only when the object is not present in the NSA catalogue. This matching of objects to NSA and SDSS is done using a $3''$ search radius for NSA and $1''$ for SDSS. The reason we allow a bit more leeway in the NSA matching is that all NSA objects are relatively large galaxies, and the likelihood for spurious matches is lower than for SDSS which contains a much broader range of star and galaxy detections.

SDSS spectroscopy is r-band limited to $r \leq 17.77$, meaning many of the galaxies in our sample do not have SDSS redshifts. We obtained a catalogue of redshifts measured with HECTOSPEC (c.o. Mike Hudson, private communication) which increases the size

of our sample with redshifts. We define Coma cluster membership based on redshift where galaxies with $0.0133 < z < 0.0333$ are considered to be Coma members. This corresponds to velocity dispersions of $\pm 3000 \mathrm{km\,s^{-1}}$.

We obtain published optical Sérsic profile fits to Coma galaxies from Simard et al. (2011). This study uses GIM2D (Simard 1998; Simard et al. 2002) to perform Sérsic fits and bulge-disk decompositions on a set of over a million galaxies from SDSS. While they perform three sets of fits ($n_b = 4$ bulge + exponential disk, free n_b + exponential disk, single component pure Sérsic model), we focus on the pure single Sérsic fits for r_e measurements in this study. From our sample of 525 galaxies with redshift (148 Coma members), we have 115 (91) after matching to the Simard et al. (2011) catalogue. The Simard et al. (2011) catalogue supplements SDSS spectroscopic redshifts with photometric redshifts, and then uses these redshift values to calculate the effective radii in kiloparsecs, which they then report in their catalogue. However, we have spectroscopic redshifts for our entire sample of galaxies which have much less uncertainty than photometric redshifts, so we correct the effective radii values reported in Simard et al. (2011) to reflect the scale at the spectroscopic redshift. Additionally, for all galaxies determined to be Coma members, we determine the kiloparsec scale based on a fixed distance to the cluster of 98kpc, since the redshift variations of galaxies within the cluster are largely due to velocity dispersions. We assume a flat ΛCDM cosmology with $\Omega_M = 0.3$, $\Omega_\Lambda = 0.7$, and $H_0 = 70\,\mathrm{km\,s^{-1}\,Mpc^{-1}}$.

Finally, we match our Coma galaxies to the catalogue of Michard & Andreon (2008), who classified hundreds of objects in the Coma cluster line-of-sight from the GMP catalogue (Godwin et al. 1983) using optical imaging.

To obtain a sample of field galaxies for comparison to our cluster sample, we turn to the Herschel Reference Survey (HRS; Boselli et al. (2010)), a study of dust in the nearby universe. The HRS includes UV imaging of 280 galaxies using GALEX. GALEX is the UV predecessor to UVIT, and provided a resolution of $\sim 5''$. While this resolution is worse than that of UVIT by a factor of four to five, the HRS sample is volume limited to $15 \leq D \leq 25\,\mathrm{Mpc}$, placing the typical HRS galaxy five times closer than Coma. This offset of image resolution and distance balances to produce the same image quality in our cluster and field samples. Cortese et al. (2012) measured structural parameters in the UV using the GALEX imaging of HRS galaxies as well as optical properties using SDSS imaging. To measure asymptotic magnitudes and effective radii of galaxies, they employed a method previously used by Gil de Paz et al. (2007) and Cairós et al. (2001) which involved measuring surface brightness profiles and subsequent flux growth curves of galaxies, extrapolating the total magnitude and determining the effective radius. This method will be discussed in more detail in chapter 3. Since the HRS sample contains galaxies in the Virgo cluster as well as field galaxies, we separate the two based on 3D

position.

Chapter 3

Methods

The surface brightness profiles of galaxies are often well-described by Sérsic profiles (Sérsic 1963). The Sérsic model is given by:

$$I(r) = I_e \exp\left\{ -b_n \left[\left(\frac{r}{r_e} \right)^{\frac{1}{n}} - 1 \right] \right\} \tag{3.1}$$

where $I(r)$ is the surface brightness at radius r, and $I_e = I(r_e)$. r_e is the effective radius (half-light radius), inside of which half of the light of the galaxy is emitted. The coefficient b_n is such that $\gamma(2n; b_n) = \frac{1}{2}\Gamma(2n)$. Quiescent, early-type galaxies are often well-described by a Sérsic profile with $n = 4$, which is de Vaucouleur's law (de Vaucouleurs 1948). Star-forming, late type galaxies are often dominated by disks which are well-described by an $n = 1$ Sérsic profile, where the Sérsic law dissolves into an exponential. Because Sérsic profiles effectively extend to infinity, it is difficult to define a true outer boundary of a galaxy by which its size can be measured. Thus, it is common to use the effective radius as a measure of galaxy size.

3.1 AUTOPROF

As mentioned in chapter 2, the effective radius measurements of HRS field galaxies made by Cortese et al. (2012) do not involve full Sérsic fits but rather measuring the surface brightness profile of a galaxy and eventually extrapolating the effective radius through a series of steps. In order to properly compare sizes of the UVIT Coma sample of galaxies to

the HRS field sample, we develop a routine akin to what was done in Cortese et al. (2012) (see also Gil de Paz et al. 2007; Cairós et al. 2001). The only difference with our method is that instead of using GALPHOT (Haynes et al. 1999) to measure surface brightness profiles as in Cortese et al. (2012), we elect to use AUTOPROF (Stone et al. 2021). AUTOPROF is a publicly available surface brightness extraction pipeline, with several modern updates to the process including methods adopted from machine learning. Given an image and a basic configuration file, AUTOPROF can measure and subtract the background, find the object centre and fit elliptical isophotes to a galaxy to extract the surface brightness profile (see Stone et al. 2021 for a full review and comparison with other photometric analysis software). Since AUTOPROF has several techniques one can choose for background measurement, it can actually measure the low UV background in our UVIT images quite well. However, we decide still to provide AUTOPROF with a background value and background scatter obtained from our own background fitting procedure.
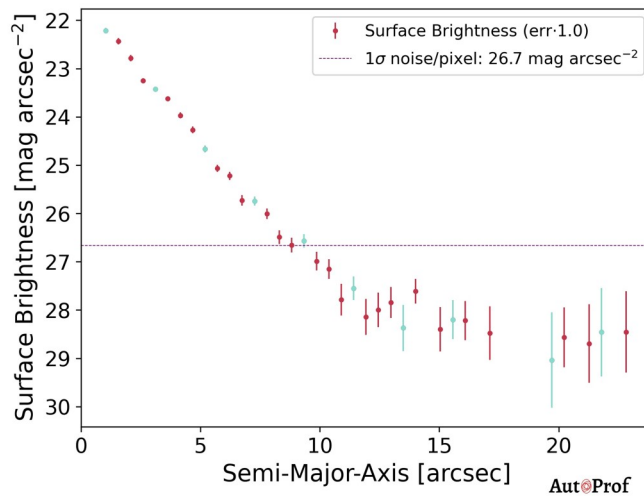
Figure 3.1: Example of a surface brightness profile output from AUTOPROF.

(a)

(b)

(c)
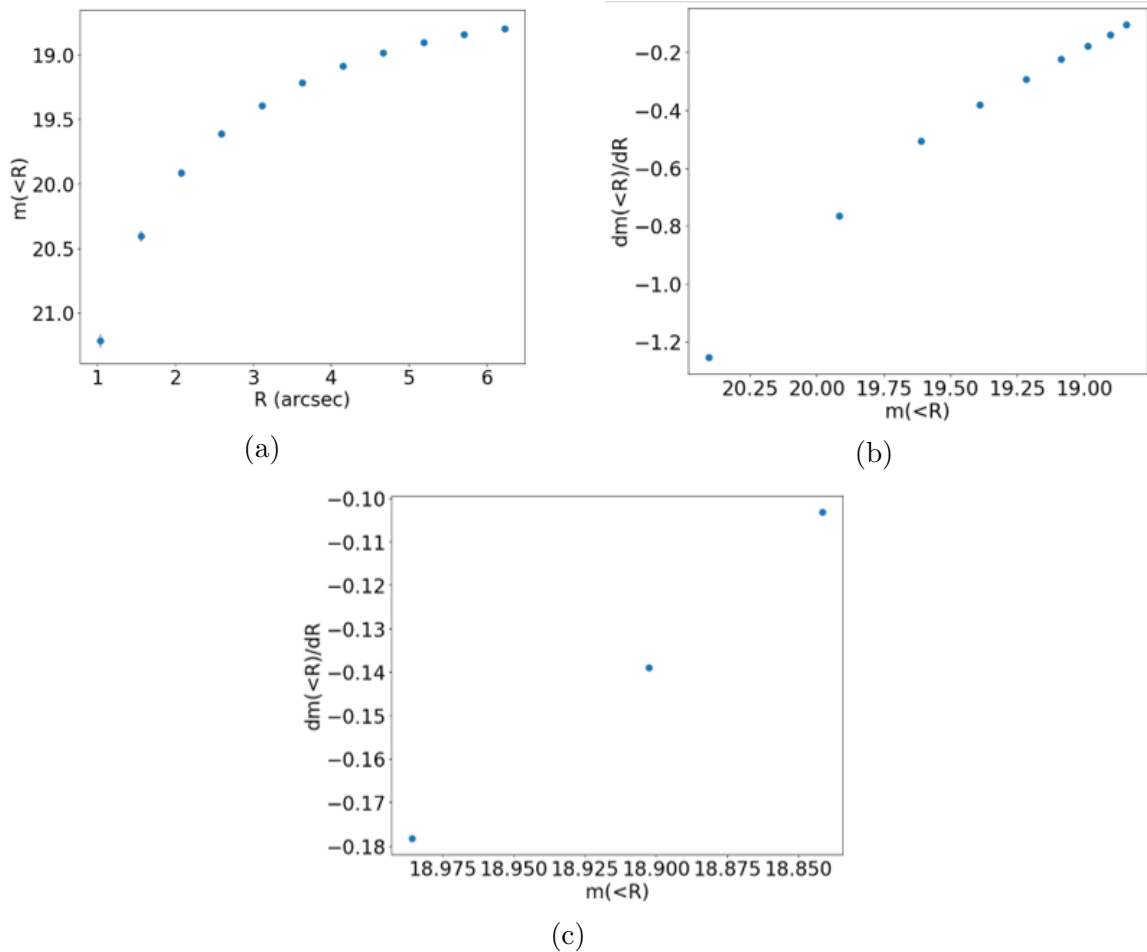
Figure 3.2: (a) Magnitude growth curve extracted from the surface brightness profile. (b) Derivative of the growth curve as a function of magnitude. (c) Same as (b) but showing just the linear region of the curve.

The output file from AUTOPROF contains a total integrated magnitude at each radial point where the surface brightness was determined, and we use this data to plot a growth curve for the galaxy, $m(< r)$ as a function or r. To extrapolate the total asymptotic magnitude from the growth curve, we first make a cut at 2.5σ above the background to remove any noise-dominated points. We then measure the slope of the growth curve, $dm(< r)/dr$, at each point and plot against the magnitude. Next we fit a straight line to the last three points in the profile, measure the reduced chi-squared statistic (χ_ν^2), and then iteratively add data points to the linear fit and calculate χ_ν^2 again at each iteration.

19

Once complete, the linear fit which minimizes χ_ν^2 is chosen as a suitable data range (with a minimum of three data points). This linear fit is then extrapolated to $dm(<r)/dr = 0$ to determine the total magnitude of the galaxy. The half light magnitude is then given by $m(r_e) = m_{tot} + 2.5log_{10}(2)$, and the half-light radius is the location at $x = r_e$ on the growth curve where $y = m(r_e)$. This process is illustrated in Figures 3.1 and 3.2, with Fig. 3.1 showing the 1D surface brightness profile output from AUTOPROF. Fig. 3.2a shows the integrated growth curve of the same galaxy, with the range of radial values extending to 2.5σ above the background. Fig. 3.2b shows $dm(<r)/dr = 0$ as a function of magnitude, with Fig. 3.2c showing the linear regime with the best χ_ν^2 value.

We tested our AUTOPROF routine on a subset of ten galaxies from the HRS sample, and found good agreement between the published values from Cortese et al. (2012) and our results using AUTOPROF.

3.2 GALFIT and MEGAMORPH

In order to properly compare UV sizes of our Coma sample to optical sizes from Simard et al. (2011), we employ MEGAMORPH (Häußler et al. 2013) to model 2D Sérsic profile fits to our galaxies. MEGAMORPH is an updated version of GALAPAGOS (Barden et al. 2012) that includes multi-wavelength capabilities. The pipeline performs source extraction (with SExtractor) on images, performs background subtraction and postage stamp cutting and then uses an updated, multi-wavelength version of GALFIT3 (Peng et al. 2002, 2010a) known as GALFITM to fit Sérsic profiles to galaxies. Herein, anytime a reference is made to the model fitting part of this pipeline we will refer to GALFIT, and any time a reference is made to steps in the pipeline leading up to the GALFIT fits, we will reference MEGAMORPH. GALFIT performs a least-squares minimization using a Levenberg-Marquardt algorithm, using the χ_ν^2 statistic to measure goodness-of-fit. The χ_ν^2 is given by:

$$\chi_v^2 = \frac{1}{N_{DOF}} \sum_{x=1}^{n_x} \sum_{y=1}^{n_y} \frac{f_{data}(x,y) - f_{model}(x,y))^2}{\sigma(x,y)^2} \tag{3.2}$$

where $f_{data}(x,y)$ and $f_{model}(x,y)$ are the flux values of a pixel in the data and model, respectively. $\sigma(x,y)$ is the uncertainty at that pixel, and N_{DOF} is the number of degrees of freedom.

Since running a least-squares routine on thousands of detections is computationally expensive, we create a target list for the GALFIT portion of the MEGAMORPH routine. The

target list includes positions of all galaxies in our Coma UVIT catalogue that are identified as galaxies by SDSS, and have redshift information. MEGAMORPH will then position match this target list to the catalogue created during the source extraction step of the pipeline, and then only run GALFIT on these objects.

We make one substantial change to the MEGAMORPH pipeline, which is to bypass the background measurement routine. While MEGAMORPH incorporates its own background measurement routine instead of allowing GALFIT to fit the sky as a free parameter, we found during trials that the background measurement routine of MEGAMORPH could not handle the extremely low background in our UVIT images, so we use a global value determined with our own background routine. We continue to hold the background fixed instead of letting GALFIT fit it.

We also run MEGAMORPH on the HRS field sample to compare full Sérsic fits of our cluster sample to the field sample.

Prior to settling on the configuration used for MEGAMORPH, we ran several tests to determine the best setup. These tests included comparing the resulting effective radius measurements when GALFIT was allowed to fit the background versus forcing GALFIT to hold the background fixed. We also developed our own wrapper for GALFIT that allowed more user overhead than MEGAMORPH, and tested runs of GALFIT with segmentation maps to make the routine more analagous to STATMORPH. The results of these tests are shown and discussed in Appendix A. We ultimately made the decision to use the MEGAMORPH runs with pre-determined global background values that are held fixed through the GALFIT fitting.

3.3   STATMORPH

In addition to running MEGAMORPH, we also run STATMORPH (Rodriguez-Gomez et al. 2019) on both the Coma cluster sample and the HRS field sample. STATMORPH is an ASTROPY (Astropy Collaboration et al. 2013, 2018)-affiliated package designed primarily for making morphoglogical measurements of galaxies such as CAS parameters and Gini-M20. However it also has the capability to fit Sérsic profiles to galaxies. The Sérsic fitting routine for STATMORPH is akin to that of GALFIT, as it uses the Levenberg-Marquardt algorithm to find the optimal fit solution. We found better success with STATMORPH when we allow the code to internally determine a weightmap for the image instead of us providing one on input. STATMORPH itself does not have a background measurement routine, so we provide a background-subtracted image on input.

3.4 Signal-to-noise

We explore the signal-to-noise (S/N) distribution of our sample. More specifically we are concerned with the S/N per pixel within the effective radius. We use this value as an estimate of how well we can fit a Sérsic model to the surface brightness profile of a galaxy, given that the accuracy of that fit depends on the distribution of the source signal. However, the success of fitting a Sérsic profile also depends on the Sérsic index (i.e. the steepness of the profile) and asymmetries in the distribution of signal across the plane of the galaxy.

We elect to take the r_e measurements from our AUTOPROF routine as our fiducial by which to compare the Sérsic r_e from GALFIT and STATMORPH. We find that this routine fails on objects that are clearly noise-dominated, potentially due to there not being enough points above the chosen noise level to extrapolate the linear region of the growth curve to find the asymptotic magnitude. We choose to exclude these from our sample for any further analysis. From here we measure the S/N per pixel on all remaining objects using the AUTOPROF effective radii and ellipticity. For each pixel, the noise measurement is given as $\sqrt{f_{pixel}}$ according to Poisson statistics, and thus the S/N is $\frac{f_{pixel}}{\sqrt{f_{pixel}}} = \sqrt{f_{pixel}}$ where f_{pixel} is the pixel flux in the original science image before background subtraction.

In Figure 3.3, we plot the ratio of effective radii measured by a Sérsic fitting code (GALFIT, STATMORPH) to the effective radii measured by the AUTOPROF growth curve method as a function of S/N per pixel. As indicated by the range of S/N values, all of our galaxies except one have an average S/N per pixel < 5 within r_e. This regime is well below the point where photon counting statistics can be reasonably approximated as Gaussian, and as such, proper handling of Poisson statistics should be used when modelling these galaxies. However, both GALFIT and STATMORPH employ least-squares algorithms that assume weights to be in the Gaussian regime. The figure also shows significant scatter in the r_e ratios below S/N per pixel of about 2, particularly in the GALFIT measurements. As such, in further analysis we are careful to consider the S/N values of individual galaxies when looking at results from measurements.

Figure 3.3: Ratio of effective radii (r_e) of Sérsic fits (GALFIT in blue, STATMORPH in orange) compared to fiducial AUTOPROF growth curve measurements, as a function of S/N per pixel, for Coma sample.

For comparison we show the same plot for the HRS field sample in Figure 3.4. The pixel size of the UVIT detector is $0.417\,\text{arcsec/pixel}$, ~ 3.6 times smaller than the GALEX pixel size of $1.5\,\text{arcsec/pixel}$ which would be present in the HRS field sample. Surface brightness in units of flux per square arcsecond is independent of distance at low-redshift; since flux and apparent area are both inversely proportional to squared distance, the two factors cancel when we consider flux per area. As such, we would expect the surface brightness per pixel differences between GALEX and UVIT to scale as the ratio of pixel sizes squared, when comparing objects with the same luminosity, physical size and exposure time. Since

within r_e we would expect our sample to be dominated by the Poisson noise of the source, we would expect the difference in signal-to-noise per pixel between GALEX and UVIT to scale by one factor of the pixel size. This assumption holds true given comparable exposure times in the UVIT and GALEX imaging. However, we have ignored the difference in telescope aperture size (37.5cm and 50cm for UVIT and GALEX respectively). As expected, the range of S/N per pixel values in Fig. 3.4 for this sample extends well beyond that of the Coma sample. However, a key thing to note is that in the higher S/N regime especially, we see good agreement with the GALFIT and STATMORPH measurements, with both tending to measure effective radii smaller than the growth curve method.
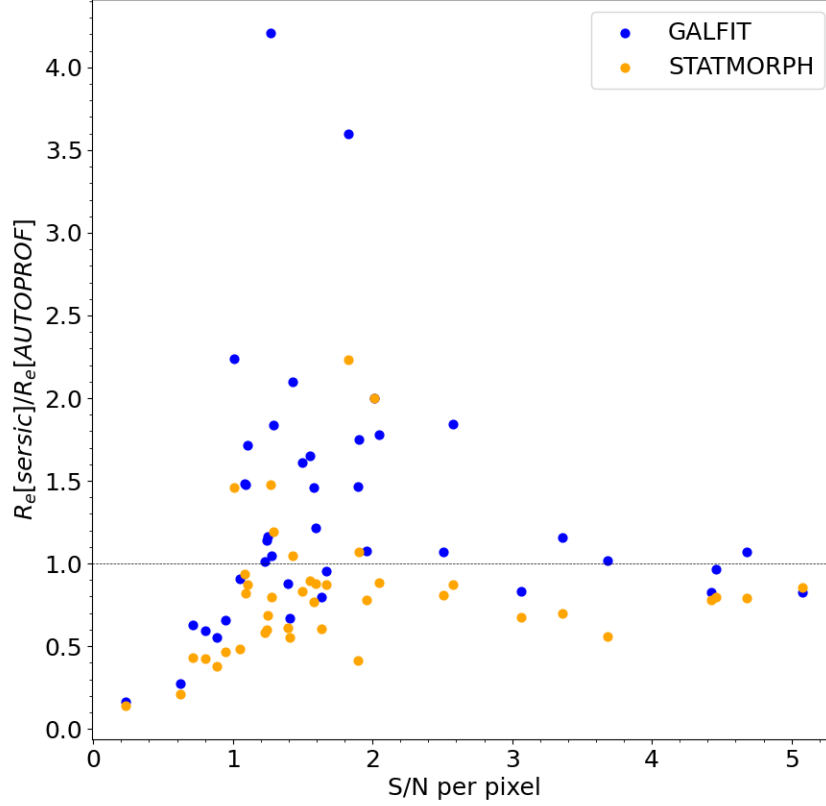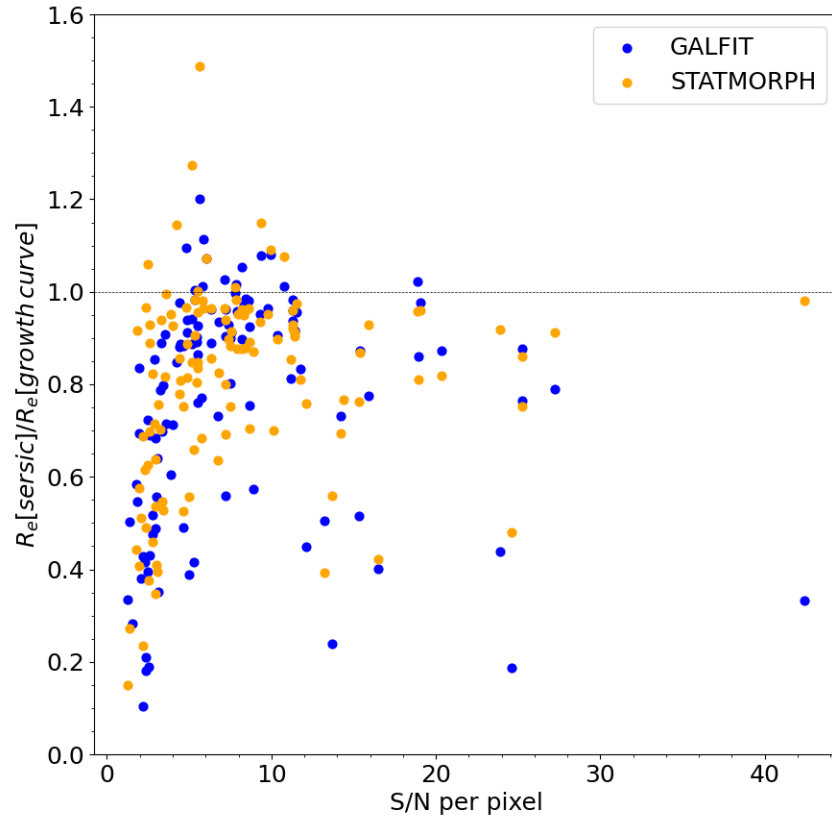
Figure 3.4: Ratio of effective radii (r_e) of Sérsic fits (GALFIT in blue, STATMORPH in orange) compared to fiducial growth curve measurements, as a function of S/N per pixel, for HRS field sample.

Chapter 4

Results

4.1   Morphological Classification of Galaxies

We begin by looking at different quantifications of morphological type of galaxies in our
UVIT sample. Smith et al. (2010) used an $NUV - i = 4.0$ colour cut to distinguish
between star-forming and quiescent galaxies, and for much of our analysis we will em-
ploy this straightforward cut. However, we also compare the bulge-to-total (B/T) values
from Simard et al. (2011) with the morphological classifications from Michard & Andreon
(2008). We apply a more general grouping to the morphological classifications to sort into
solely three categories: ellipticals, lenticulars and spirals. Michard & Andreon (2008) note
that their classifications tend to be more toward late-type galaxies than previous work
by Dressler (1980a,b), so our grouping here labels any galaxies with an elliptical flag as
elliptical (even if given an "E/S0" classification for example), then any remaining galaxies
as lenticulars if given any classification containing a "0". The remaining galaxies that have
spirals designations are put in the spiral category.

Fig. 4.1 shows UV-optical colours versus B/T ratios for all UVIT galaxies that cross-
matched with both the Simard et al. (2011) catalogue and the Michard & Andreon (2008)
catalogue. The majority of these objects have low S/N per pixel in the UVIT image or
were not successfully fit by the AUTOPROF method at all, meaning no S/N value was
determined (smaller data points). However we show this whole sample here since we are
not immediately analyzing any UV structural parameters. We see that the spiral sample
lies on the lower end of the B/T range, with almost all galaxies below 0.7. The lenticular
sample has more spread but still tends to lower values. The elliptical sample shows many
galaxies with surprisingly low B/T ratio. Since ellipticals are bulge dominated, we would

expect very high B/T fractions. The interesting result from this plot is that there may be a large sample of Coma galaxies that are in fact spiral galaxies that have red colours but retain some disk like structure in the optical.
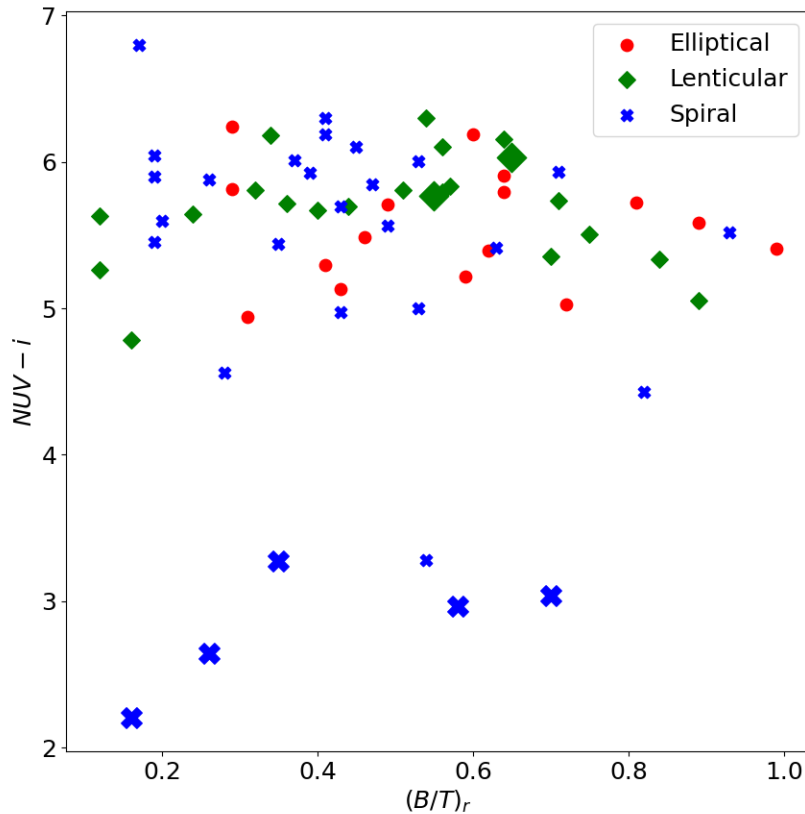
Figure 4.1: $NUV - i$ colour versus r-band B/T ratio for a sample of Coma galaxies. Elliptical galaxies are shown in red data points, lenticulars in green and spirals in blue. All classifications are from Michard & Andreon (2008). Larger data points are galaxies with UV S/N per pixel > 2, while smaller data points have UV S/N < 2 or no S/N measurement because the AUTOPROF routine failed on them.

4.2 Size Relations of Cluster and Field Galaxies

In Figure 4.2 we show the UV size-stellar mass relations for our Coma sample as well as the HRS field sample. We have made a red/blue colour cut using $NUV - i = 4.0$. Red sequence galaxies in Coma lie below the field trend, showing smaller UV effective radii for a given stellar mass bin. Blue galaxies in Coma lie on the field sequence relatively well. For this comparison, the AUTOPROF growth curve method of measuring r_e was used for the Coma sample, to properly compare with the published values from Cortese et al. (2012).
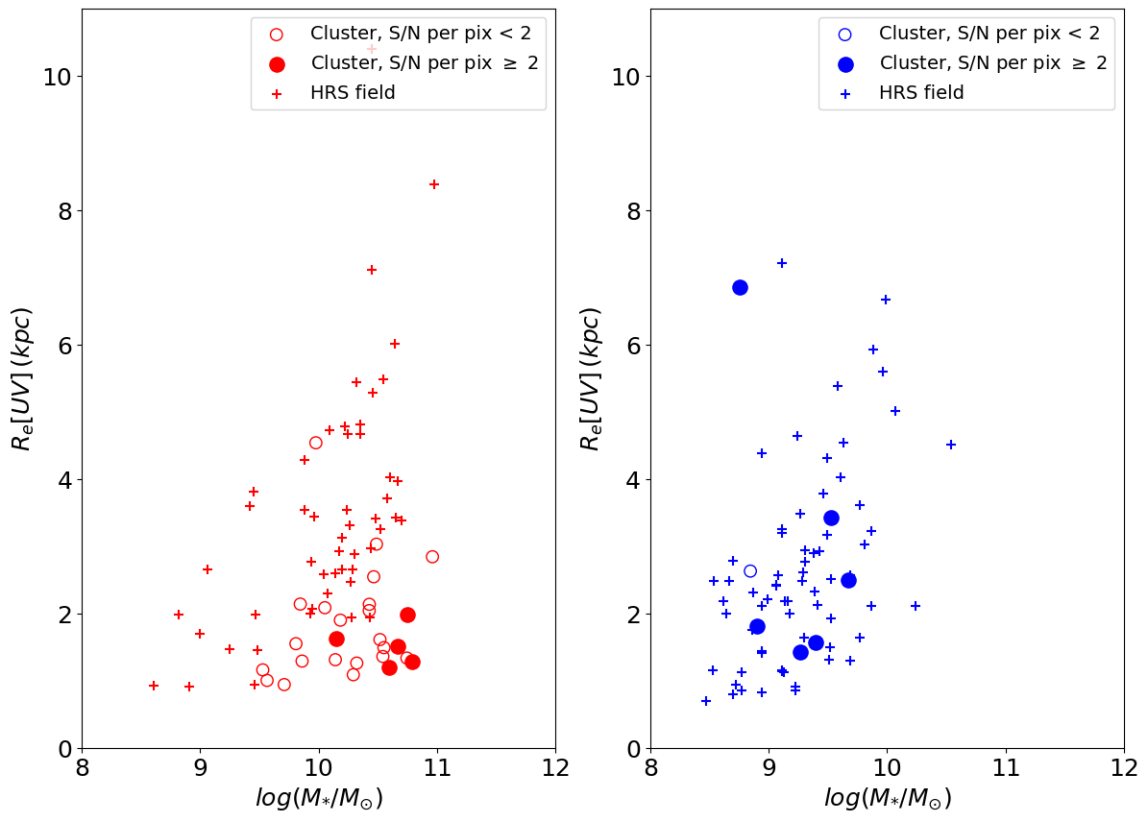
Figure 4.2: UV size-mass relation for red ($NUV - i \geq 4$, left) and blue ($NUV - i < 4$, right) galaxies in Coma sample and HRS field sample. Higher S/N galaxies in Coma are shown as larger, filled data points

Comparing the sizes of galaxies in the UV to their sizes in the optical can provide insight into how environmental mechanisms could be quenching star formation. For example,

small UV sizes relative to the optical might suggest star formation being quenched from the outside inward. To determine UV-optical size ratios for our Coma sample, we use the optical catalogue from Simard et al. (2011), who fit Sérsic profiles to galaxies using GIM2D. For a proper comparison, we use our GALFIT runs on the UVIT images, since both GALFIT and GIM2D employ full 2D Sérsic fitting. Figure 4.3 shows the UV-to-optical size ratios for the Coma sample of galaxies, colour-coded and sized according to their S/N per pixel, as a function of stellar mass. Many of the data points lie below $y = 1$ on the plot, indicating smaller UV sizes compared to r-band optical. There is some scatter, particularly in low-S/N galaxies, with several suggesting much larger UV sizes compared to optical. The solid blue line indicates the median UV-to-optical size ratio for the HRS field sample, binned by stellar mass with bins 1 dex in size. The blue shaded region shows the 68% confidence interval around the median. This data suggests the field sample of galaxies have UV sizes comparable to their optical sizes, if not marginally larger, at all stellar masses. One thing to note is that the UV and optical sizes values from the HRS sample are measured via the growth curve method, not by Sérsic fits.
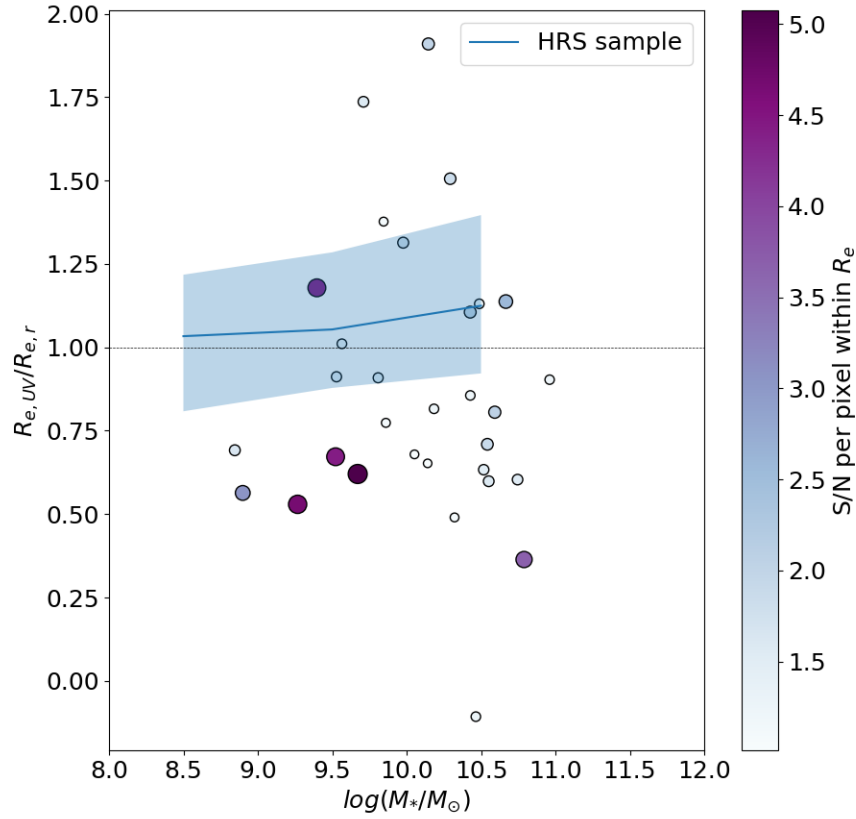
Figure 4.3: UV-optical size ratio as a function of M_*. Data points show the Coma cluster sample colour-coded and sized based on S/N per pixel. The blue line shows the median values for the HRS field sample, with the shaded area showing the 68% confidence interval.

We now move to matching individual Coma cluster galaxies to counterparts from the HRS field sample to see how the UV sizes of galaxies of similar types compare between the cluster and the field. In order to do so, we select two matching criteria, taking into consideration the small sample size, but also making an effort to ensure close matches. The two criteria are:

- $|M_{i,field} - M_{i,cluster}| = 0.5mag$

- $|(NUV - i)_{cluster} - (NUV - i)_{field}| = 0.5\,\mathrm{mag}$

Therefore, we match cluster galaxies to field counterparts based on absolute i-band magnitude and UV-optical colour, in order to then see how the UV sizes of a sample of cluster and field galaxies compare when matched one-to-one. We use absolute i-band magnitude as a proxy for stellar mass due to stellar mass data being missing for a substantial portion of our sample. We initially sought to include a third criterion where the ratio of optical sizes of the cluster and field matches must be below a certain threshold, however two issues arose. The first issue was that the optical sizes of the Coma sample are measured via 2D Sérsic fits from Simard et al. (2011) and the HRS field sample via the growth curve method of Cortese et al. (2012). Secondly, matching to the Simard et al. (2011) catalogue also limits our final sample, since there is not a 100% overlap between their catalogue and ours. We ran the matching routine with the optical size criterion included and noted there was very little difference in the final results, especially in the star-forming galaxies, so we have elected to exclude it to increase our sample size and ensure any bias from directly comparing two different methods of measuring optical sizes is mitigated. These results are shown in Appendix B for the AUTOPROF/growth curve method, GALFIT and STATMORPH.

To explore the results of matching cluster galaxies to field counterparts, we first take a close look at the set of galaxies with S/N $\geq$ 2. In Figure 4.4, we plot the cluster-to-field UV size ratios for these galaxies against their $NUV - i$ colour. We show each possible match that satisfies both constraints for a given galaxy to show the spread of potential matches. We highlight the rankings of matches based on data point size, with the best match having the largest data point. Fig. 4.4 shows results using the growth curve method. We show results from GALFIT and STATMORPH in Appendix B.

From Fig. 4.4, we see a trend with redder cluster galaxies tending to have more potential field matches with larger UV sizes. This trend carries right through to the red sequence, where we see five red cluster galaxies with small UV sizes relative to their field matches. We will explore the nature of these red galaxies further in section 4.4.
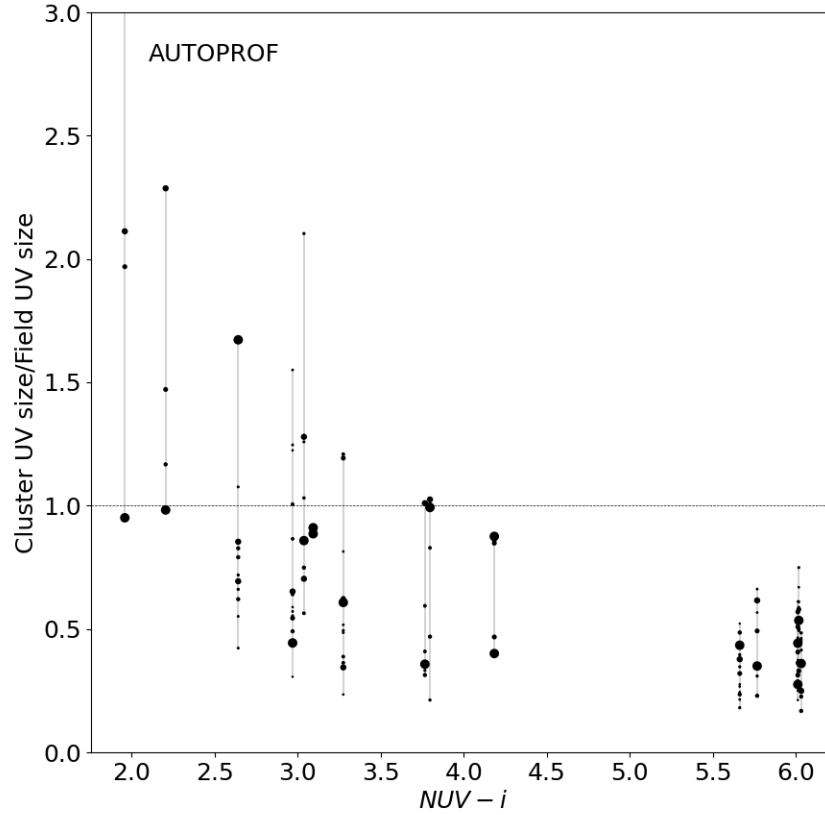
Figure 4.4: Ratios of Coma galaxy UV sizes (r_e) to the sizes of their field counterparts after matching as a function of absolute i-band magnitude. Only galaxies with S/N per pixel > 2 are shown. Data points are sized based on the ranking of the match, i.e. the largest data point is the best match, while the smallest data point is the worst match, relative to the matches for that galaxy.

Figure 4.5 shows the results of matching cluster to field galaxies based on the UV-optical colour and absolute i-band magnitude criteria for all galaxies in the sample, but now only showing the best field match to each cluster galaxy. We show the results using each of our three methods for measuring r_e; STATMORPH, GALFIT and the AUTOPROF/growth curve method. For the red sequence galaxies in the sample, there is substantial difference in the scatter between the three methods. As for blue galaxies, there is more scatter in the
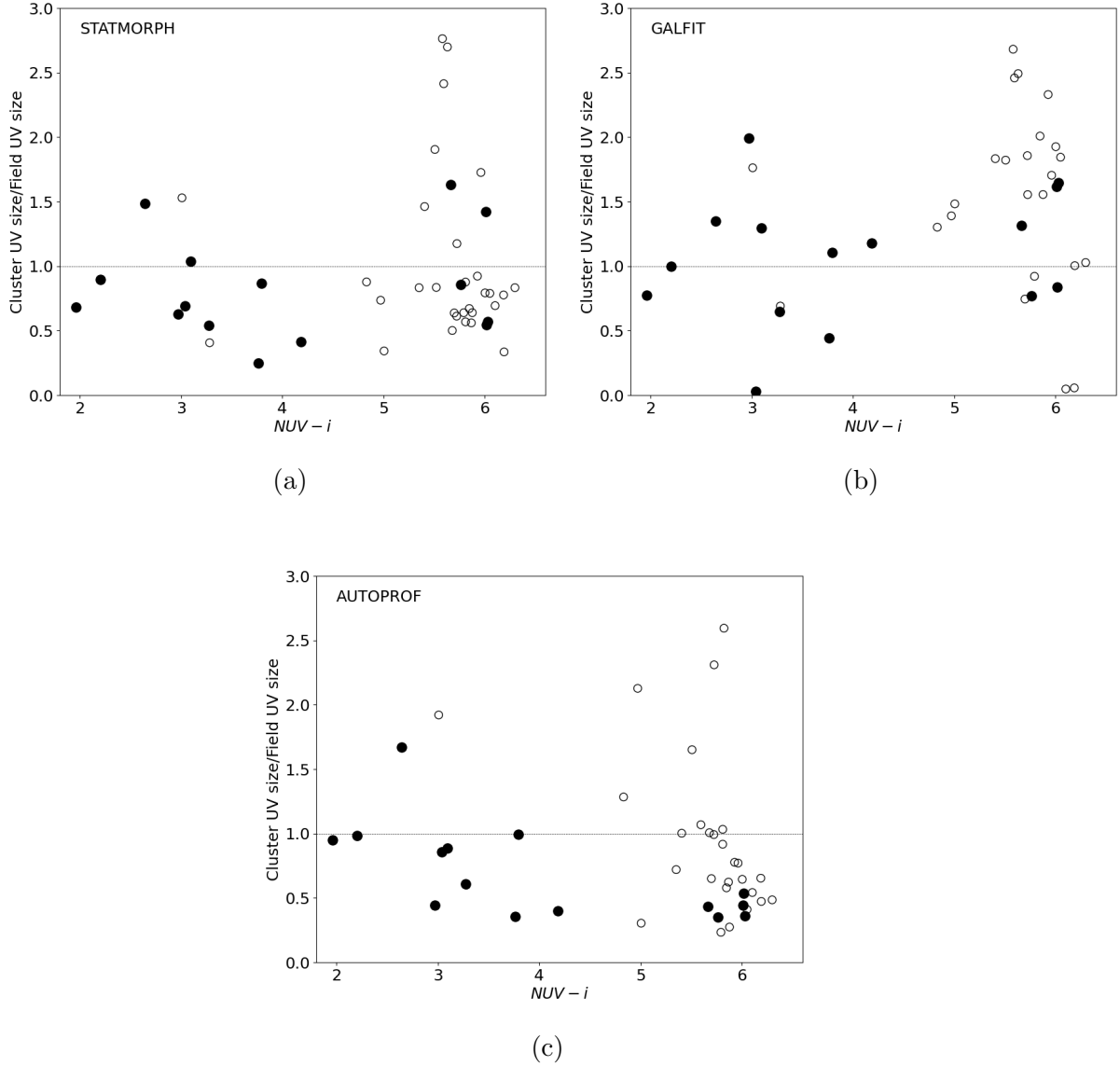
Figure 4.5: Ratios of Coma galaxy UV sizes (r_e) to the sizes of their field counterparts as a function of $NUV - i$ colour. UV r_e are determined for both the cluster and field sample via STATMORPH (a), GALFIT (b) and the AUTOPROF/growth curve method (c). Larger filled data points are galaxies with S/N per pixel ≥ 2 while smaller, open points are for S/N per pixel < 2

results for the GALFIT method than the other two methods. This is somewhat expected, as we note that Figs. 3.3 and 3.4 show that GALFIT tends to measure larger r_e than the fiducial growth curve method for the cluster, and measure smaller r_e than the fiducial in the field sample. On the contrary, the the STATMORPH results tend to measure smaller r_e compared to the fiducial in both the cluster and field sample, and by a similar amount at higher S/N. As such, we see very similar results between STATMORPH and the growth curve method, particularly in the higher S/N galaxies.

These results provide more clear evidence to truncated UV sizes in cluster galaxies than what was determinable from Fig. 4.2. We see smaller UV sizes in cluster galaxies for much of our high S/N sample, and a trend where redder galaxies shown even smaller sizes.

Table 4.1: Coma cluster galaxies with S/N per pixel $\geq$ 2

ID	RA	DEC	z	M_i	$NUV - i$	Notes
SDSS J130140.90+281456.6	195.549	28.173	0.0310	-15.45	0.96	[5]
SDSS J130238.33+282720.5	195.660	28.456	0.0186	-16.30	1.33	[5]
GMP 1582	195.549	28.173	0.0299	-19.56	1.96	[1]
GMP 2599	195.141	27.638	0.025	-20.03	2.2	[1,3]
GMP 1576	195.553	28.215	0.0273	-20.2	2.64	
GMP 3071	194.984	27.747	0.0298	-18.78	2.97	[2]
GMP 2923	195.034	27.773	0.0289	-18.44	3.04	[2]
SDSS J130221.45+282254.1	195.589	28.382	0.0195	-17.23	3.09	
GMP 2910	195.039	27.866	0.0177	-19.82	3.27	[1,2,3]
SDSS J130119.31+275137.6	195.331	27.861	0.0274	-18.55	3.77	
GMP 2316	195.26	27.775	0.0174	-17.43	3.8	
GMP 2333	195.253	27.906	0.0193	-17.4	4.18	
GMP 2374	195.234	27.791	0.0266	-22.57	4.19	[1,2,5]
SDSS J130208.66+282313.5	195.536	28.387	0.0253	-21.18	5.66	[4]
GMP 2815	195.069	27.968	0.0155	-20.53	5.77	[4]
SDSS J130147.01+280542.0	195.446	28.095	0.0194	-21.12	6.01	[4]
GMP 2516	195.178	27.972	0.0213	-21.43	6.02	[4]
GMP 3178	194.942	27.857	0.027	-20.37	6.03	[4]

[1] Identified as a stripping candidate by Roberts & Parker (2020)
[2] Identified as a stripping candidate by Yagi et al. (2010)
[3] Identified as a stripping candidate by Smith et al. (2010)
[4] Red galaxy with potential disk or spiral structure
[5] Not matched with HRS field galaxy

Table 4.1 lists the 18 objects in our final catalogue that are members of Coma and have S/N per pixel of at least 2. These are the objects that we will primarily consider for further analysis, since our tests of S/N suggest that this is the minimum cut necessary to be able to put trust in the results of the size measurements from the three measurement methods. 11 of these galaxies are considered star-forming based on our $NUV - i$ cut. Two more have slightly redder colours, but we include them in the star-forming sample due to the fact that they are clear outliers from the red sequence. Three of the star-forming galaxies did not match to galaxies from the HRS sample, but we include them here in case they are of interest for further qualitative analysis. We order the galaxies in Table 4.1 by colour, from bluest to reddest, and also indicate which star-forming galaxies have been previously

identified as gas stripping candidates by Roberts & Parker (2020), Yagi et al. (2010) or Smith et al. (2010). After these considerations, we are left with seven star-forming galaxies not previously identified as stripping candidates, as well as five red galaxies that may show disk-like or spiral structure.

4.3 Stripping Candidates

Here we will qualitatively look at the six star-forming galaxies in our sample that have been identified as stripping candidates in previous works. This will provide a qualitative baseline for assessing the remaining star-forming galaxies that have not previously been identified as stripping candidates. In Figure 4.6 we show these six galaxies in a stacked (NUVF1 + FUVF2 + NUVF3 + NUVF5) UVIT image on the left, and an NUV GALEX image on the right. We see that while the GALEX data has higher S/N, the much higher resolution of UVIT images allows stripping features to be identified in more detail. We plot the vector pointing toward the cluster centre in green.

Of the six galaxies shown in Fig. 4.6, we see clear asymmetric UV emission and/or bright UV knots in GMP 1582, 2374 and 2599. These features can be interpreted as being indicative of ram-pressure stripping, and are also seen in the optical (GMP 1582, 2374 and 2599; Roberts & Parker 2020), Hα (GMP 2374; Yagi et al. 2010) and once again the UV (GMP 2599; Smith et al. 2010). The other three galaxies (GMP 2910, 2923 and 3071) were all identified as stripping candidates by Yagi et al. (2010) using Hα imaging. In particular, the galaxy GMP 2910 (D100) shows a massive, narrow stream of gas detectable in Hα (shown in Figure 1.3). Higher S/N UV imaging from GALEX also showed this tail in the UV. With our lower S/N but higher resolution UVIT imaging, it is difficult to identify the tail in GMP 2910 "by-eye" without further analysis. In UVIT imaging, GMP 2923 and 3071 both show disk-like structure, but again there is no immediately identifiable tail of stripped gas seen. It is possible that this stripped gas is only faintly observable in the UV and would require deeper imaging.
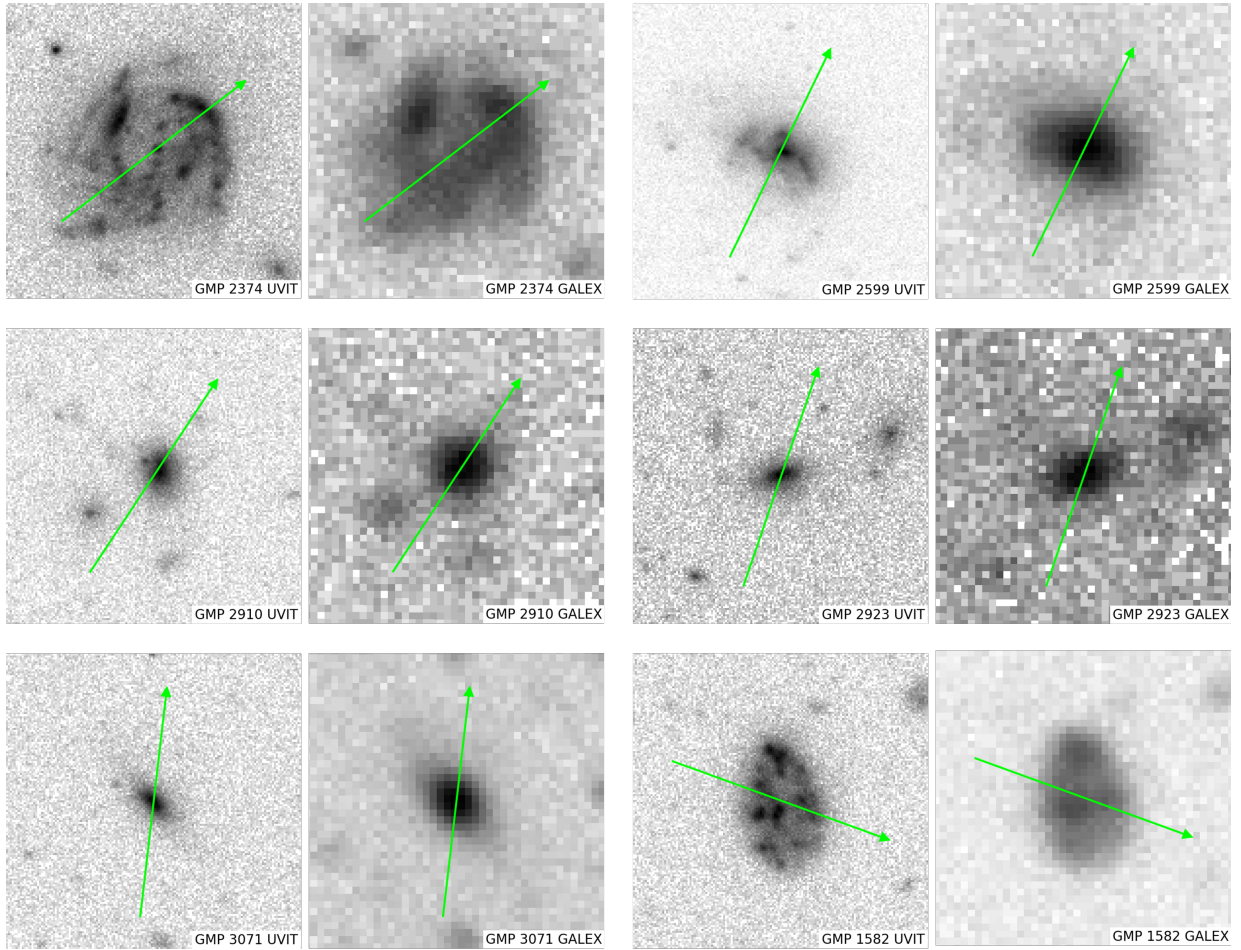
Figure 4.6: Previously identified stripping candidates in Coma sample. All images are 30 kpc squares. Stacked UVIT images are shown alongside GALEX NUV images. The green vector points toward the cluster centre. In all images north is up and east is to the left

We make special note of the galaxy GMP 2374, also known as NGC 4911. This galaxy is one of the largest and brightest spirals in Coma, and has been the focus of several previous studies. It is thought that NGC 4911 is interacting with its nearest neighbour, a lenticular companion to the southwest (Bravo-Alfaro et al. 2000). This could partially explain the orientation of the stripped Hα emission mapped by Yagi et al. (2010) shown in Figure 4.7, where the companion galaxy is visible in the centre of the image. In the UVIT image, however, the most prominent stripping feature appears directed to the southeast, along

the vector pointing away from the cluster centre. This is more indicative of ram-pressure stripping, and it is very likely this galaxy is currently undergoing ram-pressure stripping and interacting with its nearest neighbour as it approaches the centre of the cluster.
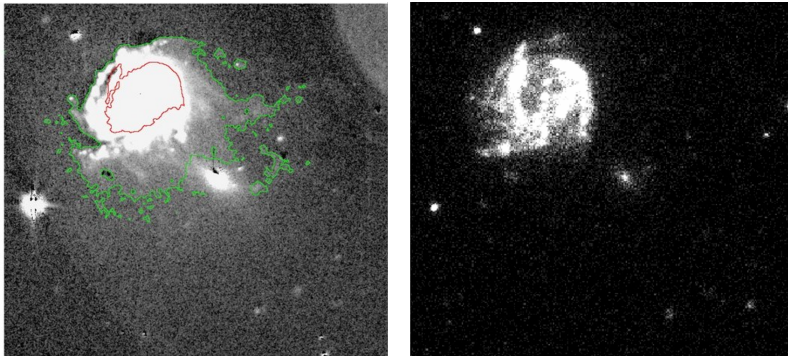
Figure 4.7: (left) From Yagi et al. (2010) (Figure 4): Hα image of NGC 4911 with green contour showing isophote of $2.5 \times 10^{-18}\,\mathrm{erg\,s^{-1}\,cm^{-2}\,arcsec^{-2}}$, and red contour showing the isophote representing the SDSS r-band Petrosian r_{50}. (right) UVIT stacked UV image of the same galaxy. North is up and east is to the left

We further study the images of the remaining blue galaxies in the sample, those that have not been previously identified as stripping candidates. The low S/N of even these brightest galaxies make it difficult to perform a robust analysis to look for stripping features. One objects stands out however: GMP 1576. This galaxy has not been previously identified as a stripping candidate, and is actually one of the brightest star-forming galaxies in our sample. We show this galaxy in Figure 4.8 in an NUV image alongside an r-band image. We plot a contour on the NUV image at $26\,\mathrm{mag/arcsec^2}$, corresponding to 3σ above the background, which outlines asymmetric UV emission in two places: right along the vector pointing toward the cluster, and another tail pointing toward the south. This is an indication of the galaxy possibly undergoing ram-pressure stripping as it moves away from the cluster centre, leading to the asymmetric features pointing back toward the centre.
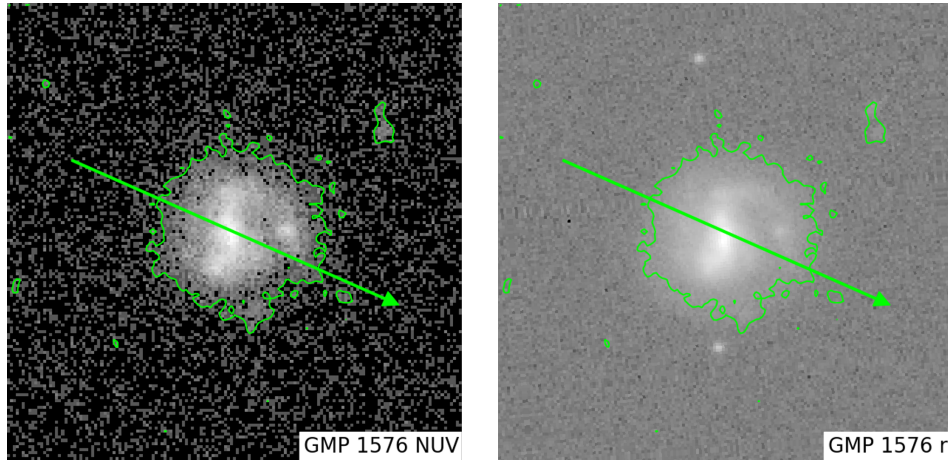
Figure 4.8: GMP 1576 shown in NUV and r. The green contour in both images outlines an isophote at $26\,\mathrm{mag/arcsec^2}$ in the NUV. The green vector points toward the cluster centre. North is upward and east is to the left

4.4 Red Sequence Galaxies

Our sample also contains five red sequence galaxies with S/N per pixel > 2, as shown in Fig. 4.4. All five of these galaxies show smaller UV sizes in Coma as compared to their field counterparts. While this would be expected for early-type galaxies with little to no remaining star formation and primarily central UV emission, it is interesting to study the images of each of these galaxies in the UV and optical to see their structure. Three of these five red galaxies were classified as lenticular galaxies by Michard & Andreon (2008), and the other two were not classified. Additionally, four of the five galaxies are in the Simard et al. (2011) catalogue with g and r-band bulge-disk decompositions. The four galaxies had bulge-to-total (B/T) ratios in the r-band between 0.47 and 0.65, again placing them in the lenticular category. A summary of these parameters is shown in Table 4.2.

Table 4.2: Red sequence galaxies in Coma sample with S/N per pixel > 2

ID	Hubble Type [1] Classification	r-band B/T ratio [2]
SDSS J130208.66+282313.5	-	0.47
GMP 2815	SA0/a	0.55
SDSS J130147.01+280542.0	-	0.61
GMP 2516	SB0/a	-
GMP 3178	SA0/a	0.65

[1] Michard & Andreon (2008).
[2] Simard et al. (2011).

Further, in Figure 4.9 we show each of the five red disk galaxies in both a stacked UV image and the SDSS r-band. In each case, a clear disk is visible in the r-band, while the UV emission is more centralized. No stripping features are clearly seen in any of the five cases.
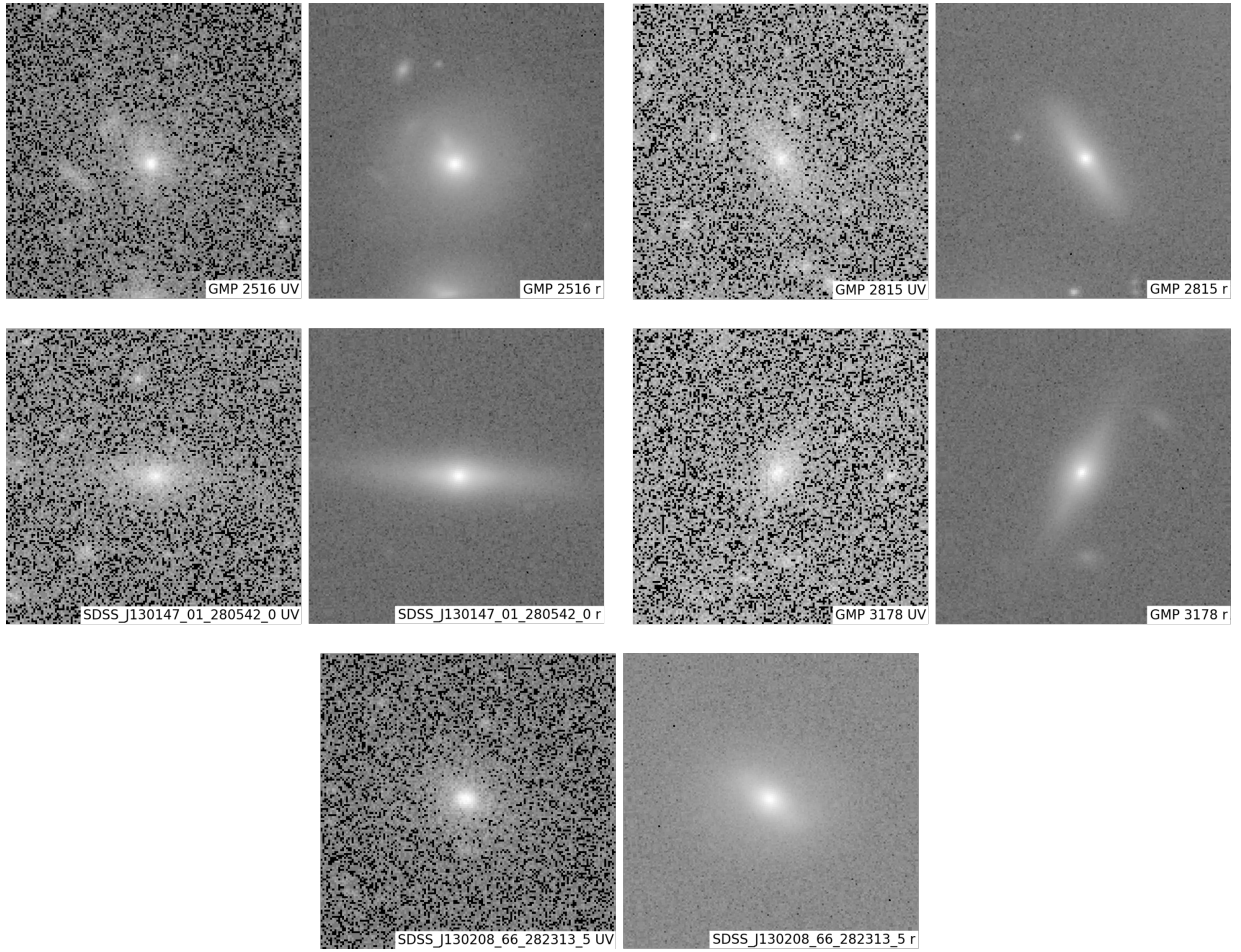
Figure 4.9: Five red galaxies in our sample with S/N per pixel > 2 showing disk structure in r-band (right images) and more centralized UV emission (left images).

Fig. 4.1 showed that a substantial proportion of UVIT galaxies in our sample were red in UV-optical colour, but classified as spirals and with low B/T ratios. While most of these galaxies cannot be well studied with the UVIT data given the low S/N per pixel, we look for more interesting examples of red disks or spirals in our sample. A famous example in Coma is NGC 4921. NGC 4921 is an archetypal "anemic" spiral (van den Bergh 1976), because its surface brightness is rather diffuse, and it is mostly devoid of star formation, yet retains clear spiral arms. Observations have indicated that the galaxy is not only undergoing ram-pressure stripping, but also has some of its stripped gas re-accreting onto the galactic disk (Bravo-Alfaro et al. 2000; Cramer et al. 2021). NGC 4921 lies right at the edge of our Coma5 field of view, so all that can really be seen in the UVIT image is an area of bright UV emission along the leading edge of the galaxy. This is confirmed when looking at a lower resolution GALEX image, which shows only very faint spiral structure in the UV but bright UV emission along the leading edge. This could be indicative of recent ram-pressure induced star formation occurring in an otherwise relatively dead galaxy.

We find three additional red galaxies in our sample showing spiral and/or bar structure in the optical. Each of these galaxies have low S/N in the UV, and thus were not discussed in detail when comparing cluster and field sizes. We show these galaxies here simply as a qualitative example of red, anemic spiral galaxies in the Coma cluster. Figure 4.10 shows a stacked UV and stacked *gri* images for GMP 3068, 3238 and 2355. These three galaxies were classified as SBa, SBa and SAb respectively by Michard & Andreon (2008).
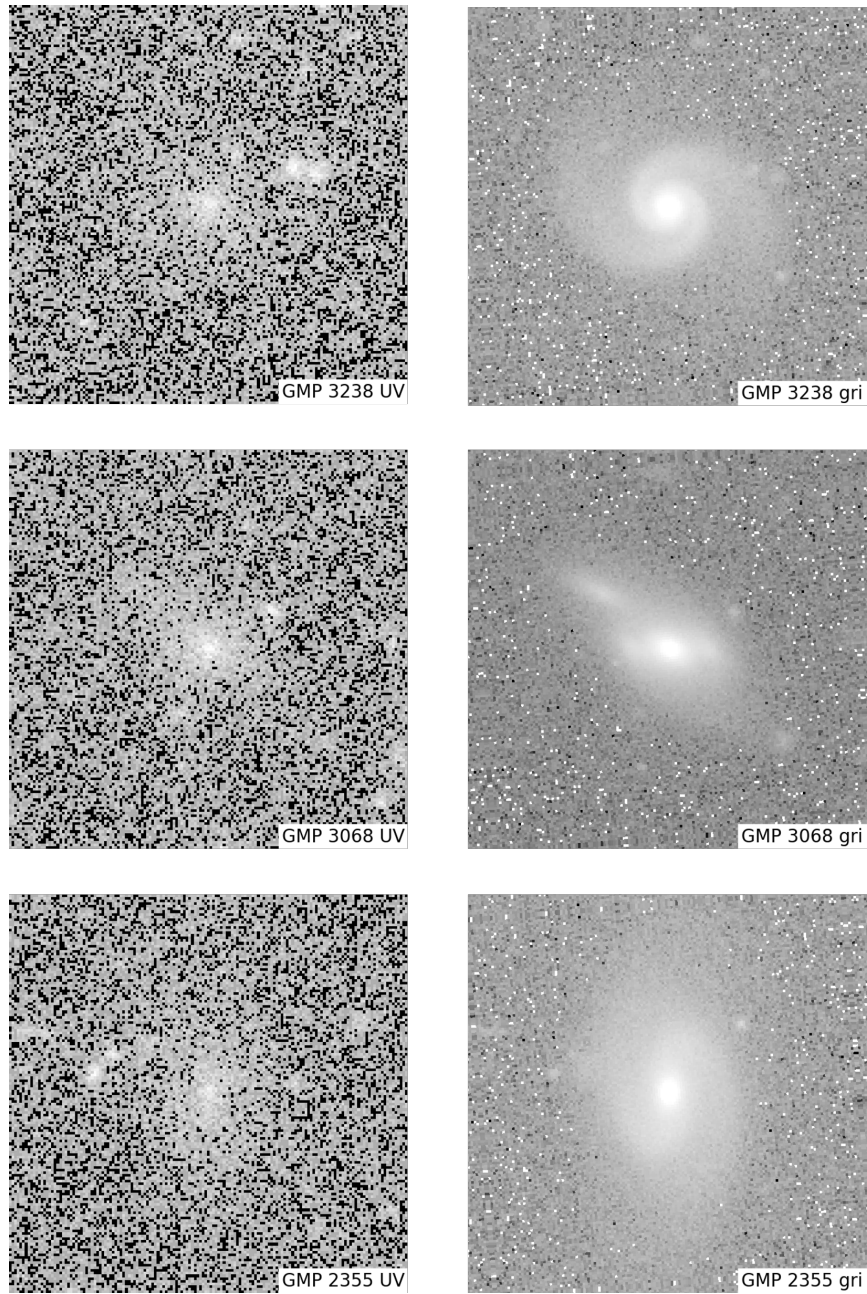
Figure 4.10: Examples of additional red galaxies in Coma with visible spiral structure in optical bands. These galaxies were not shown in Figs. 4.4 or 4.9 due to them having S/N per pixel < 2. Left images show stacked UV image and right images show stacked *gri* SDSS images.

43

Chapter 5

Discussion

In this thesis we have made use of wide-field, high-resolution UV imaging of the Coma cluster to measure UV sizes of a sample of cluster galaxies. Combining our results with several catalogues from the literature, we have identified and measured galaxies with a variety of different morphologies, from very blue star-forming galaxies, to passive early-types. In our sample of bright star-forming galaxies we have qualitatively discussed the morphology seen in six galaxies previously identified as candidates for ram-pressure stripping, and shown how the enhanced spatial resolution of UVIT data allows the identification of UV knots and subtle asymmetries that were harder to identify with previous UV imaging from GALEX.

5.1   UV sizes in cluster galaxies

We have matched the brightest galaxies in our cluster sample to field counterparts, and found consistently smaller UV sizes in the cluster compared to the field. There also is a trend whereby redder galaxies show even smaller relative UV sizes. This trend extends beyond the blue cloud and into the red sequence, where we find several disky red galaxies with only centralized UV emission.

Cortese et al. (2012) look at trends in structural parameters in the UV and optical in the HRS. Instead of directly comparing cluster to field galaxies, they separate galaxies based on HI content using the HI-deficiency parameter (Cortese et al. 2011; Haynes & Giovanelli 1984). HI-deficient galaxies are likely to be members of the Virgo cluster in the HRS sample. They find that HI-deficient galaxies show marginally smaller effective radii in

UV bands as compared to the optical. More striking however, is the observation that, with increasing stellar mass, galaxies show decreasing effective surface brightness in the UV, and increasing effective surface brightness in the optical. By comparing sizes measured in the g, NUV and FUV bands to the i-band, Cortese et al. (2012) find a clear trend with smaller UV-optical sizes measured in galaxies that are more HI-deficient. They measure sizes using both effective radii and isophotal radii and find a stronger correlation with the latter. This leads to a look at a colour-stellar mass relation, separating the colours inside and outside of the optical effective radius, shown in Figure 5.1. The right panel of Fig. 5.1 shows the difference in $NUV - i$ colour between the inside and outside, meaning positive numbers indicate redder colours inside the effective radius than outside and negative indicates bluer colours inside than outside. At all stellar masses, the average HI-normal HRS galaxy shows slightly redder colours inside the effective radius than outside. However, at least at low stellar mass, HI-deficient galaxies tend to show redder colours outside the effective radius. These results coupled together provide significant evidence for an outside-in quenching mechanism such as ram-pressure stripping being responsible for the removal of HI gas. Since the HRS contains galaxies in the Virgo cluster, these results suggest ram-pressure stripping to be a dominant mechanism in the cluster opposed to an inside-out mechanism such as tidal interactions.

Using r-band effective radii and magnitudes from Simard et al. (2011), we perform this same analysis on our sample of UVIT galaxies. With the effective radius being identical to the half-light radius, the inside and outside r-band magnitudes are determined simply by adding $2.5log_{10}(2)$ to the total r-band magnitudes. To determine the inside and outside NUV magnitudes, we find the data point in our AUTOPROF surface brightness profiles at $r = r_{e,r}$ and use the integrated magnitudes to find the inside magnitude, and then calculate the outside magnitude from the inside and total magnitudes. We find that all nine galaxies show redder colours outside the r-band effective radius, with higher stellar mass galaxies actually showing even redder colours. The average colour difference between the inside and outside, $(NUV - i)_{in} - (NUV - i)_{out}$, for these nine galaxies is -1.1. The magnitude of this colour difference is consistent with the results of Cortese et al. (2012) for HI-deficient galaxies and provides evidence for an outside-in quenching mechanism impacting the evolution of these galaxies. Figure 4.4 could also be interpreted as evidence for outside-in quenching. While bluer cluster galaxies have smaller UV disks relative to their field counterparts, this trend is even more extreme for redder cluster galaxies that show much smaller UV disks relative to the field. An outside-in quenching mechanism would grab hold of the bluest galaxies with substantial ongoing star formation, and begin to strip away the gas from the disk from the outside, leaving a smaller UV disk and a redder galaxy over time as the star formation fades away.
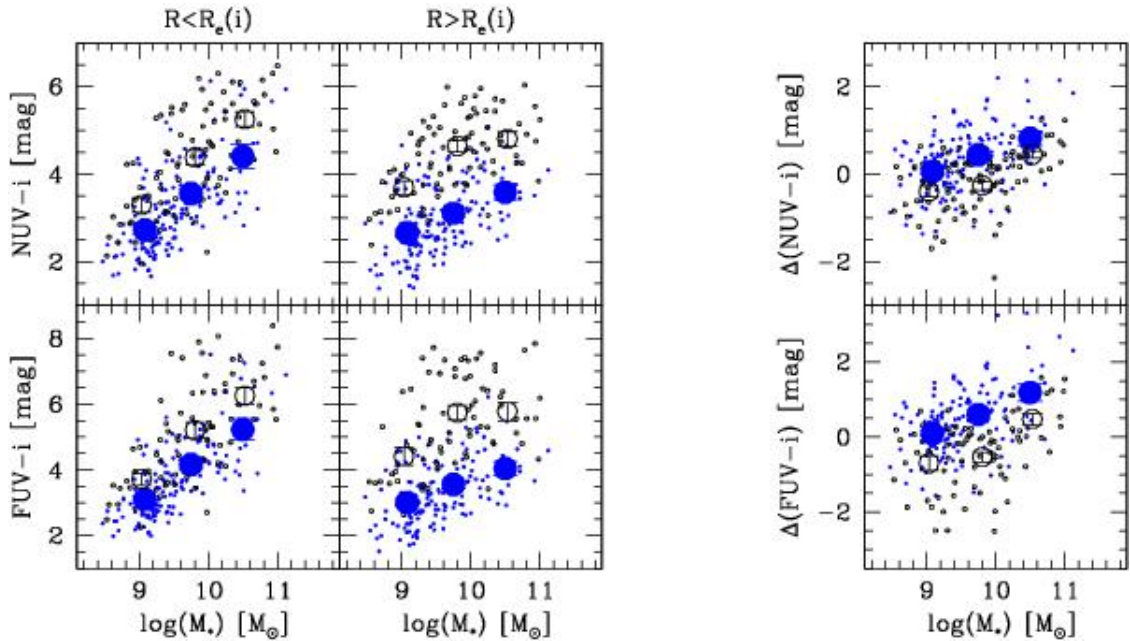
Figure 5.1: Fig. 8 from Cortese et al. (2012), showing colour-stellar mass relations for the HRS sample for the region within the optical effective radius and beyond the optical effective radius. Filled circles show H I-normal galaxies while open circles are H I-deficient. The large circles show averages in stellar mass bins.

5.2 Red Spiral Galaxies

Our main method for separating blue star-forming galaxies from red, passive ones is a colour magnitude relation (CMR) of $NUV - i$ vs i which plots a clear red sequence of galaxies underlined by a blue cloud. However, using the work of Michard & Andreon (2008), we note that a substantial fraction of galaxies in our red sequence have late-type morphologies. This is further evidenced using the optical B/T fits from Simard et al. (2011) which shows that many of our red sequence galaxies are not bulge dominated. Studying the UV images of many of these supposed red spiral galaxies alongside optical imaging does in fact show disk-like structure and occasionally very pronounced spirals, with UV emission mainly concentrated in the centre of the galaxy. We now move to a discussion surrounding this red spiral sample, and how its existence and prevalence compares to other studies of similar populations.

Wolf et al. (2009) studied red spiral populations in the cluster complex A901/2, building off work by Wolf et al. (2005) who used SED fitting to outline a population of "dusty red spirals." Other works have identified passive spiral galaxies, or anemic spirals (van den Bergh 1976; Poggianti et al. 1999, 2004; Goto et al. 2003a). The results of Wolf et al. (2009) show that populations dubbed "optically passive spirals" and those dubbed "dusty red spirals" overlap greatly. They called into question the characteristics of these populations of galaxies, and found that "dusty red spirals" are not in fact entirely passive like traditional early-type galaxies with aging stellar populations. Red spirals do in fact show significant rates of star formation, though their SFR is about four times less on average than blue star-forming galaxies in the A901/2 sample (Wolf et al. 2009). While the obscuring of star formation in "dusty red galaxies" is not any more drastic than in blue star-forming galaxies, the lower rates of star formation coupled with dust reddening put the observed colours of these galaxies into the same range as passive early-type galaxies.

Furthermore, Wolf et al. (2009) showed that using a CMR relation to split blue and red galaxies, and then using that cut to label blue galaxies as star-forming and red galaxies as quiescent typically will underpredict the fraction of star-forming galaxies in a cluster, since the "dusty red galaxies" will be placed into the red/quiescent category. If we assume red spirals to have ongoing star formation in Coma, we see this same trend in our sample, with the majority of galaxies being placed on the red sequence, but that red sample having a broad range of morphologies as outlined by Michard & Andreon (2008). We seek here to roughly determine the fraction of red spirals in Coma and compare to the results from Wolf et al. (2009) and other works to see how the frequencies of different morphologies of red galaxies in Coma compare to other cluster samples and to the field.

In Wolf et al. (2009), the red spiral fraction of galaxies in the cluster sample with $\log M_*/M_\odot > 10$ is ~ 0.30; that is, classified as Sa, Sb, Sc or Irr and have red colours as defined by a CMR cut. In the four cluster cores in their sample, ~ 0.20 of galaxies with $\log M_*/M_\odot > 9$ are red spirals. The Michard & Andreon (2008) data focuses on a region in the core of the Coma cluster. Their catalogue provides B-band magnitudes and B-R colours, which we plot in a CMR in Figure 5.2 for all galaxies identified as Coma members by the morphological classification system of Michard & Andreon (2008). We choose to make a colour cut under the red sequence at $B - R = 1.6$. We find that the fraction of red spirals in this sample is 0.16 for all galaxies.
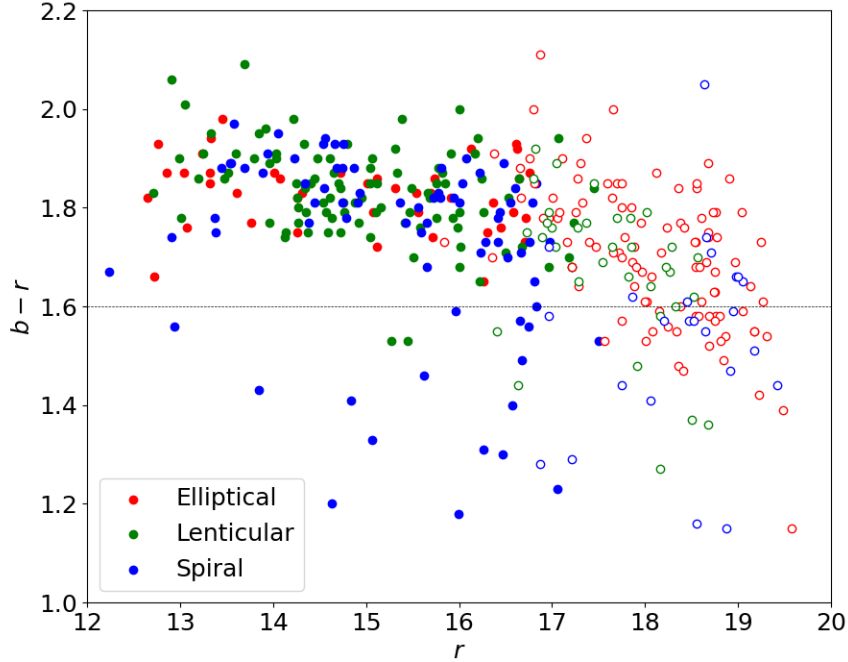
Figure 5.2: CMR for sample of Michard & Andreon (2008) identified as Coma members based on morphology. We distinguish between ellipticals, lenticulars and spirals as in Fig. 4.1. Filled circles are galaxies identified as giants, while open circles represent dwarfs.

If we narrow the Michard & Andreon (2008) sample to include only galaxies in the area covered by our UVIT sample (without cuts based on S/N, etc.), we find more drastic results. Here we have included optically-detected galaxies that are not detected in our UV sample, using a 3σ limit calculated in the same manner as our 5σ limit in section 2 to define their NUV magnitudes. Making a colour cut at $NUV - i = 4.0$ as in Smith et al. (2010), we find the fraction of red spirals to be 0.38 of all galaxies. We note that if we use a 5σ limit instead of 3σ there is almost no change in our results. We also removed any non-detections that resulted in unphysical UV-optical colours, as these galaxies likely did have matching UVIT detections but failed to match up based on our matching criteria. In Figure 5.4 we show the fraction of red spirals in bins of i-band magnitude, 1 mag in width, with errorbars, with colour cuts made at both $NUV - i = 4.0$ and $NUV - i = 5.0$. This plot shows that the fraction of red spirals is not strongly dependent on magnitude. There is an increase in the red spiral fraction at lower magnitudes, but uncertainties are large.

48

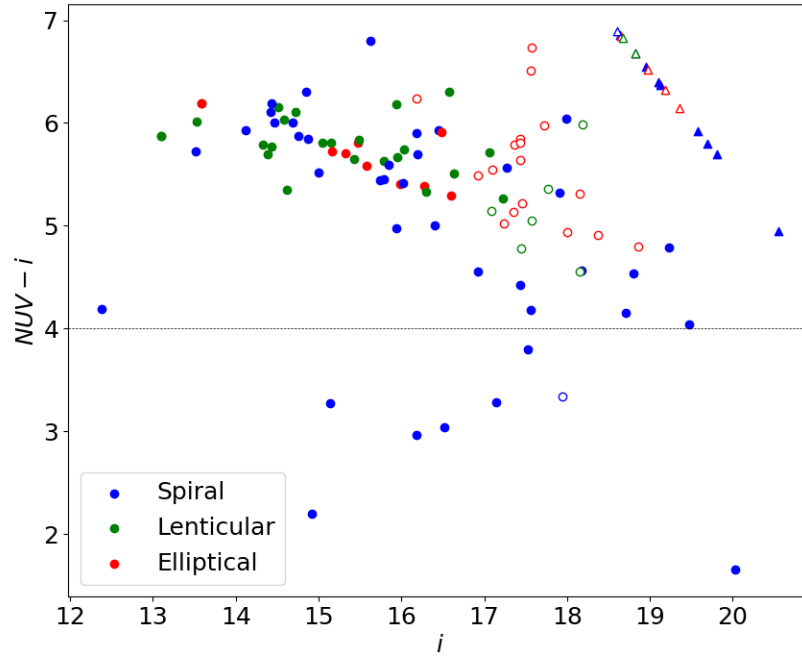At fainter magnitudes the red spiral fraction is more sensitive to the choice of $NUV - i$ colour cut.

Figure 5.3: UV-optical CMR for Coma sample of galaxies that are in Michard & Andreon (2008) catalogue. Symbols are as in Fig. 5.2. Triangle markers represent UV non-detections with magnitudes defined using a 3σ limit. Filled markers are giant galaxies while unfilled markers are dwarfs.
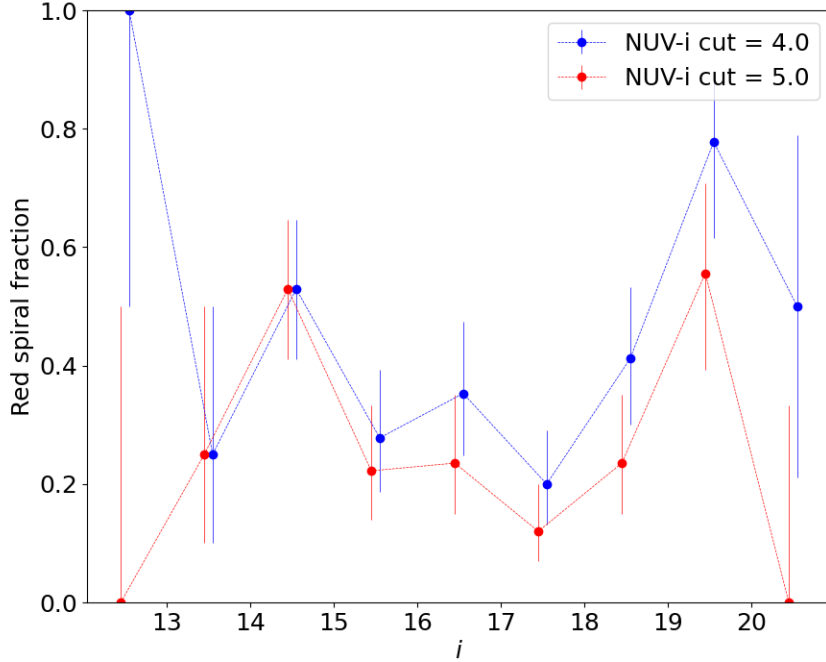
Figure 5.4: Fraction of red spirals as a function of i-band magnitudes, in bins of 1 mag. The blue points show the fractions if a cut is made at $NUV - i = 4.0$ and the red points if a cut is made at $NUV - i = 5.0$.

It is evident that the Coma cluster does in fact have a significant population of red spiral galaxies, similar to the population seen in A901/2. The existence of these galaxies has been theorized as a transition population between active blue spiral galaxies and passive lenticular ones. Moran et al. (2006) studied the cluster Cl 0024+17 at $z \sim 0.4$ using GALEX FUV imaging. They found that passive spirals in the cluster sample exhibited bluer rest-frame $FUV - V$ colours than early-type red galaxies, though redder than blue spirals. This is seen in our UVIT sample in Fig. 5.3 where we see several spiral galaxies in an intermediate region between the red sequence and the blue cloud. This also means that moving the $NUV - i$ cut drastically changes the fraction of red spirals in the sample. Moran et al. (2006) compared $FUV - V$ colours with Balmer line absorption for passive and active spirals, as shown in Figure 5.5. They plot evolutionary tracks using the populations synthesis code of Bruzual & Charlot (2003), which show that there is a possible evolutionary track from active to passive spirals through starvation. They also note that dust alone is

not enough to explain the redder colours of passive spirals, but that some reduced rate of star formation is necessary. This is complimentary to the work of Wolf et al. (2009) who point out the coupling effect of dust and reduced star formation to explain "dusty red galaxies."
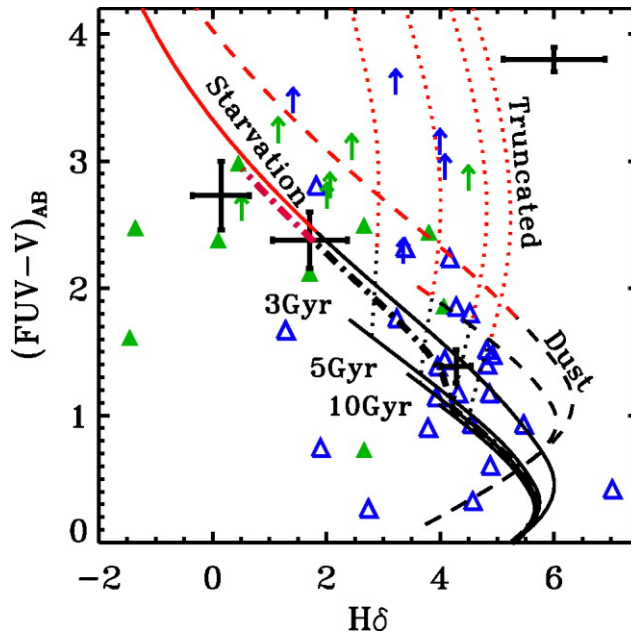

Figure 5.5: Figure 3 from Moran et al. (2006) showing rest frame $FUV - V$ versus $H\delta$. Passive spirals are shown in green triangles and active spirals in blue triangles. Various evolutionary tracks for different star formation histories are shown as lines.

5.3 Future Work

The Coma cluster is a massive, rich cluster and allows for an in-depth probe into cluster-driven environmental effects on member galaxies. In our sample here we have identified candidates for ram-pressure stripping, showing agreement to stripping studies from the literature using a range of emission to probe possible stripping events (Smith et al. 2010; Yagi et al. 2010; Roberts & Parker 2020). Beyond that, we have shown that Coma has a significant fraction of red spiral galaxies in its core region, using the classifications of Michard & Andreon (2008). These results show the complexity of environment-drive quenching processes in cluster environments. Though significant evidence exists for gas stripping,

tidal effects and starvation/strangulation in clusters, it remains unclear what the dominant driver is in shutting down star formation in cluster galaxies.

We have shown that UV emission is a powerful tool in mapping out recent and ongoing star formation in galaxies, and we consider now what future work could be done to study the Coma cluster even more robustly in the UV.

We consider the Cosmological Advanced Survey Telescope for Optical and Ultraviolet Research (CASTOR). CASTOR is a Canadian-led project that will be the next generation of UV space telescopes, filling in the UV gap while missions such as the James Webb Space Telescope, Euclid and Roman Space Telescope probe the optical and infrared regimes. CASTOR will have a deep survey with 100-hour exposures that will probe depths to $u \sim 29$, with image quality of 0.15" FWHM.

We have shown in this work that a minimum S/N per pixel of 2 within the effective radius is necessary to make measurements of the size of a galaxy. This value is a function of both flux and the size of the object. We look to scale the depth achievable with CASTOR compared to UVIT for constant (total) S/N. The aperture size of CASTOR is 100cm, compared to 37.5cm for UVIT. This amounts to a greater collecting area on CASTOR by a factor of $\left(\frac{100}{37.5}\right)^2 \approx 7$. In terms of exposure times, our UVIT pointing had exposures of about 2000s, while the CASTOR deep survey will be 360000s, meaning an exposure time increase of 180x. We assume the noise is dominated by source noise, since the UV background is small. As such $S/N \propto \sqrt{FD^2t}$, where F is the flux of the object being imaged, D is the telescope aperture diameter, and t is the exposure time. Therefore,

$$\frac{\mu_{castor}}{\mu_{uvit}} = \frac{\sqrt{F_{castor}D_{castor}^2 t_{castor}}}{\sqrt{F_{uvit}D_{uvit}^2 t_{uvit}}} \tag{5.1}$$

The S/N per pixel (μ_p) scales roughly as $\frac{\mu}{\sqrt{A}}$, where A is the area over which the S/N (μ) is being averaged, in number of pixels. For an object with fixed physical size at a fixed distance, its area in pixels is its area in square arcseconds divided the pixel scale squared. Therefore, to see how much fainter an object with fixed size can be to achieve the same μ_p in UVIT and CASTOR, we make the following calculation:

$$\frac{\mu_{p,castor}}{\mu_{p,uvit}}\frac{\sqrt{A_{castor}}}{\sqrt{A_{uvit}}} = \frac{\sqrt{F_{castor}D_{castor}^2 t_{castor}}}{\sqrt{F_{uvit}D_{uvit}^2 t_{uvit}}}$$

$$\frac{F_{uvit}}{F_{castor}} = \frac{A_{uvit}D_{castor}^2 t_{castor}}{A_{castor}D_{uvit}^2 t_{uvit}}$$

$$\frac{F_{uvit}}{F_{castor}} = \frac{p_{castor}^2 D_{castor}^2 t_{castor}}{p_{uvit}^2 D_{uvit}^2 t_{uvit}} \qquad (5.2)$$

$$\frac{F_{uvit}}{F_{castor}} = \frac{(0.1)^2}{(0.417)^2}(7)(180)$$

$$\frac{F_{uvit}}{F_{castor}} = 72.5$$

$$m_{uvit} - m_{castor} = -2.5\log{(72.5)} = 4.7$$

This means that with CASTOR, a depth 4.7 magnitudes deeper than UVIT can be achieved with the same S/N per pixel. We note, however, that this is a faint-end limit to the CASTOR depth, as objects at the fainter end of the CASTOR regime are likely to be background-dominated. However, most of the objects in UVIT have source-dominated noise in the UV.

In Figure 5.6 we show the effective radii for all of our UVIT objects that were measured with AUTOPROF plotted against their magnitudes. We then show contours of S/N per pixel. Note that the calculation of these contours employs two generalizations. The first is that the S/N per pixel is calculated by taking the total S/N and dividing by $\sqrt{A}$ where A is the number of pixels. This gives values close to those determined by taking the average S/N value at each pixel, but the two methods vary more for objects with higher Sérsic indices. Secondly, we calculate the S/N per pixel within the effective radius using a circular aperture with $r = r_e$. As such, there is some scatter between the S/N contours and the values measured for our UVIT galaxies. The contours for UVIT are shown in red, and the contours for the CASTOR deep survey are shown in blue.
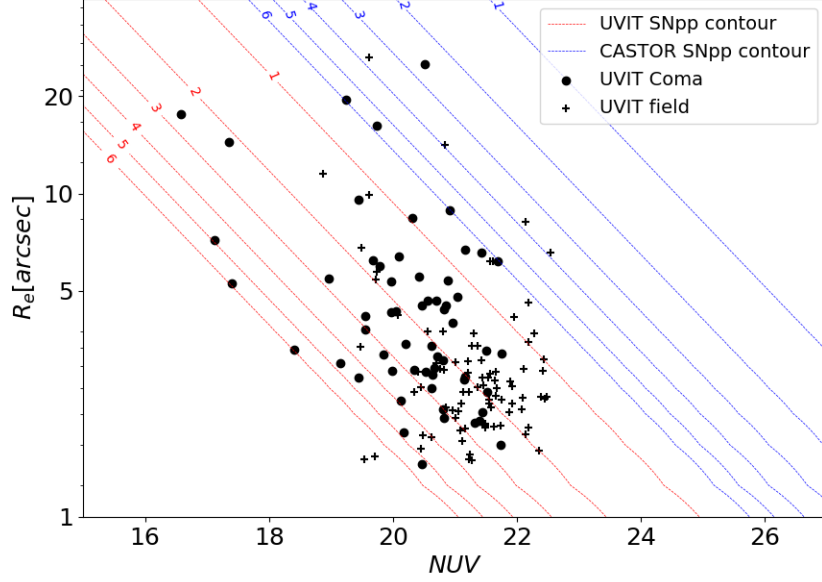
53

Figure 5.6: Effective radius versus NUV mag for UVIT galaxies measured with AUTOPROF. Coma cluster members are shown as points while field (background) galaxies are shown as crosses. Red contours show the calculated S/N per pixel within r_e for UVIT and blue contours show the same for CASTOR.

In total, our UVIT sample contains 146 spectroscopically confirmed Coma galaxies with $m_{NUV} \leq 24.5$. 110 of these galaxies are in the "Coma5" region and 36 in the "Coma7" region. This leads to surface densities of 688 and 225 galaxies per square degree, respectively. The "Coma5" region is close to the cluster centre, and thus is richer. Based solely on the Coma galaxies shown in Fig. 5.6, the CASTOR deep survey could fit all galaxies except one with a S/N per pixel greater than 5, which would allow for size measurements with much less uncertainty than S/N per pixel of 2. We caution that Fig. 5.6 does not show all 146 Coma members in our detection catalogue, as some galaxies were not successfully fit using our AUTOPROF/growth curve method. However, in many cases, these galaxies were both at the small and faint end of our sample, and thus did not have enough data points to fit the linear regime of the growth curve. As such, these galaxies would be expected to lie in the regime where the CASTOR deep survey can image them with sufficient S/N per pixel. Very few galaxies had S/N per pixel > 5 in UVIT imaging, so if S/N per pixel > 5 can be achieved with CASTOR for most of the sample, then the resulting sample of galaxies with

robust size measurements would be increased by about two orders of magnitude compared to this study. Even in the case that a S/N per pixel of just 2 can be achieved, the sample of galaxies with size measurements would be increased by an order of magnitude. We can see from Fig. 5.6 that at $m_{NUV} = 23.5$, CASTOR should provide a S/N per pixel of at least 2 for galaxies with sizes up to $r_e \sim 10''$, or ~ 4.8kpc at the distance of Coma. This size limit covers the majority of galaxies in the cluster, and we note that most galaxies of larger sizes are also much brighter than this limit. Given the CASTOR field-of-view covers an area of ~ 0.25 sq. deg, the whole virialized region of Coma could be covered with 15 CASTOR pointings.

Chapter 6

Summary and Conclusions

In this thesis we have studied a sample of galaxies in the Coma cluster through their ultraviolet emission at a greater resolution than previously possible. By measuring the sizes of galaxies in the cluster, we have identified galaxies that are likely being subject to environmental effects in the cluster.

- We find that the typical galaxy in the UVIT sample has low S/N per pixel within r_e which makes using existing Sérsic profile fitting codes difficult, since these codes make use of Gaussian statistics, but the UVIT data is very much in the Poisson regime (see Figure 3.3). This has made measuring accurate UV sizes of a reasonable sample of galaxies difficult, though we are able to come up with a small sample of mainly blue galaxies that remain large and bright in our sample. We plot size-stellar mass relations for our cluster galaxies against field galaxies from the HRS and find that while the bright blue galaxies in our sample fit the sequence well, the bright red galaxies tend to show smaller UV sizes than the field (Figure 4.2). In addition, most of the higher-S/N cluster galaxies show small UV-optical size ratios compared to the field sample (Figure 4.3).

- To take a closer look at the differences in UV sizes between cluster and field galaxies, we have matched up each of our higher-S/N cluster galaxies with field counterparts, based on absolute i-band magnitude and $NUV - i$ colour. We find that typically, galaxies in the cluster sample show smaller UV sizes as compared to their field counterparts. In fact, there is a trend where redder cluster galaxies have smaller UV sizes relative to their field counterparts than bluer cluster galaxies. This extends into the red sequence for five galaxies we identify as red disks (Figure 4.4).

- In our sample of high-S/N blue galaxies, we find six galaxies that have been previously identified as ram-pressure stripping candidates by previous works, and qualitatively study their images. Further, we identify one additional galaxy, GMP 1576, as a possible stripping candidate due to its overall asymmetric UV emission and tails oriented near the vector pointing toward the cluster centre. This galaxy had not been previously identified as a stripping candidate.

- Beyond the expected blue, star-forming galaxies, we consider red sequence galaxies identified as spirals by Michard & Andreon (2008). We see clear spiral or disk structure in some of these galaxies in the optical, with UV emission more centralized. These galaxies are examples of those that may still be star-forming at lower rates due to starvation from the cluster, and are having their residual star formation obscured by dust, making them appear red. They may also fit into the definition of anemic spirals. We find that Coma contains a substantial fraction of red spirals, a few times higher than the number of blue spirals. This is in line with previous works looking at red spirals in clusters (e.g. Wolf et al. 2009).

We find our results are consistent with previous studies that have shown evidence for environmental effects shaping the evolution of galaxies in cluster (e.g. Moran et al. 2006; Cortese et al. 2012). Small UV sizes of cluster galaxies as compared to their optical sizes and the UV sizes of field galaxies implies that star formation is being shut down in cluster galaxies from the outside-in which is consistent with models of ram-pressure stripping. Furthermore, the abundance of red galaxies with spiral structure indicates that more passive processes like starvation are slowly shutting down star formation in galaxies without disrupting their overall morphology.

Our analysis has shown that UV imaging is a powerful tool to trace environmental effects of dense environments on the evolution of galaxies. In order to reach more robust conclusions about the prevalence of different quenching mechanisms, a larger sample with deeper imaging is needed. This will be achievable with the CASTOR deep survey, and the resulting data will allow a substantial jump in the advancement of studying galaxy evolution through UV emission.

References

Aaronson M., Cohen J. G., Mould J., Malkan M., 1978, ApJ, 223, 824

Abadi M. G., Moore B., Bower R. G., 1999, MNRAS, 308, 947

Ahumada R., et al., 2020, ApJS, 249, 3

Alberts S., Adams J., Gregg B., Pope A., Williams C. C., Eisenhardt P. R. M., 2022, ApJ, 927, 235

Astropy Collaboration et al., 2013, A&A, 558, A33

Astropy Collaboration et al., 2018, AJ, 156, 123

Bahcall N. A., Cen R., 1993, ApJL, 407, L49

Baldry I. K., Balogh M. L., Bower R. G., Glazebrook K., Nichol R. C., Bamford S. P., Budavari T., 2006, MNRAS, 373, 469

Balogh M. L., Morris S. L., Yee H. K. C., Carlberg R. G., Ellingson E., 1997, ApJL, 488, L75

Balogh M. L., Schade D., Morris S. L., Yee H. K. C., Carlberg R. G., Ellingson E., 1998, ApJL, 504, L75

Balogh M. L., et al., 2016, MNRAS, 456, 4364

Barden M., Häußler B., Peng C. Y., McIntosh D. H., Guo Y., 2012, MNRAS, 422, 449

Behroozi P. S., Wechsler R. H., Conroy C., 2013, ApJ, 770, 57

Bekki K., 2014, MNRAS, 438, 444

Bertin E., Arnouts S., 1996, A&AS, 117, 393

Blanton M. R., Kazin E., Muna D., Weaver B. A., Price-Whelan A., 2011, AJ, 142, 31

Blumenthal G. R., Faber S. M., Primack J. R., Rees M. J., 1984, Nature, 311, 517

Böhringer H., Chon G., Fukugita M., 2017, A&A, 608, A65

Boselli A., et al., 2010, PASP, 122, 261

Boselli A., Cortese L., Boquien M., Boissier S., Catinella B., Gavazzi G., Lagos C., Saintonge A., 2014, A&A, 564, A67

Bower R. G., Benson A. J., Malbon R., Helly J. C., Frenk C. S., Baugh C. M., Cole S., Lacey C. G., 2006, MNRAS, 370, 645

Bravo-Alfaro H., Cayatte V., van Gorkom J. H., Balkowski C., 2000, AJ, 119, 580

Bruzual G., Charlot S., 2003, MNRAS, 344, 1000

Bundy K., Ellis R. S., Conselice C. J., 2005, ApJ, 625, 621

Butcher H., Oemler A. J., 1984, ApJ, 285, 426

Cairós L. M., Vílchez J. M., González Pérez J. N., Iglesias-Páramo J., Caon N., 2001, ApJS, 133, 321

Cole S., 1991, ApJ, 367, 45

Cortese L., Gavazzi G., Boselli A., 2008, MNRAS, 390, 1282

Cortese L., Catinella B., Boissier S., Boselli A., Heinis S., 2011, MNRAS, 415, 1797

Cortese L., et al., 2012, A&A, 544, A101

Cramer W. J., Kenney J. D. P., Sun M., Crowl H., Yagi M., Jáchym P., Roediger E., Waldron W., 2019, ApJ, 870, 63

Cramer W. J., et al., 2021, ApJ, 921, 22

De Lucia G., Weinmann S., Poggianti B. M., Aragón-Salamanca A., Zaritsky D., 2012, MNRAS, 423, 1277

Di Matteo T., Springel V., Hernquist L., 2005, Nature, 433, 604

Dorman B., O'Connell R. W., Rood R. T., 1995, ApJ, 442, 105

Dressler A., 1980a, ApJS, 42, 565

Dressler A., 1980b, ApJ, 236, 351

Driver S. P., et al., 2022, MNRAS, 515, 2138

Drory N., Salvato M., Gabasch A., Bender R., Hopp U., Feulner G., Pannella M., 2005, ApJL, 619, L131

Efstathiou G., 2000, MNRAS, 317, 697

Einstein A., 1917, Sitzungsberichte der Königlich Preußischen Akademie der Wissenschaften (Berlin, pp 142–152

Faber S. M., et al., 2007, ApJ, 665, 265

Fontana A., et al., 2004, A&A, 424, 23

Gil de Paz A., et al., 2007, ApJS, 173, 185

Giovanelli R., Haynes M. P., 1985, ApJ, 292, 404

Godwin J. G., Metcalfe N., Peach J. V., 1983, MNRAS, 202, 113

Gómez P. L., et al., 2003, ApJ, 584, 210

Goto T., et al., 2003a, PASJ, 55, 757

Goto T., Yamauchi C., Fujita Y., Okamura S., Sekiguchi M., Smail I., Bernardi M., Gomez P. L., 2003b, MNRAS, 346, 601

Greggio L., Renzini A., 1990, ApJ, 364, 35

Gunn J. E., Gott J. Richard I., 1972, ApJ, 176, 1

Hammer D. M., Hornschemeier A. E., Salim S., Smith R., Jenkins L., Mobasher B., Miller N., Ferguson H., 2012, ApJ, 745, 177

Häußler B., et al., 2007, ApJS, 172, 615

Häußler B., et al., 2013, MNRAS, 430, 330

Haynes M. P., Giovanelli R., 1984, AJ, 89, 758

Haynes M. P., Giovanelli R., Salzer J. J., Wegner G., Freudling W., da Costa L. N., Herter T., Vogt N. P., 1999, AJ, 117, 1668

Hopkins P. F., Quataert E., Murray N., 2012, MNRAS, 421, 3522

Hopkins P. F., Kereš D., Oñorbe J., Faucher-Giguère C.-A., Quataert E., Murray N., Bullock J. S., 2014, MNRAS, 445, 581

Jaffé Y. L., et al., 2018, MNRAS, 476, 4753

Jenkins A., Frenk C. S., White S. D. M., Colberg J. M., Cole S., Evrard A. E., Couchman H. M. P., Yoshida N., 2001, MNRAS, 321, 372

Kaiser N., 1986, MNRAS, 222, 323

Kauffmann G., White S. D. M., Heckman T. M., Ménard B., Brinchmann J., Charlot S., Tremonti C., Brinkmann J., 2004, MNRAS, 353, 713

Kawinwanichakij L., et al., 2017, ApJ, 847, 134

Kolcu T., Crossett J. P., Bellhouse C., McGee S., 2022, MNRAS,

Lewis I., et al., 2002, MNRAS, 334, 673

Marcolini A., Brighenti F., D'Ercole A., 2003, MNRAS, 345, 1329

Martin D. C., et al., 2005, ApJL, 619, L1

McCarthy I. G., Frenk C. S., Font A. S., Lacey C. G., Bower R. G., Mitchell N. L., Balogh M. L., Theuns T., 2008, MNRAS, 383, 593

Michard R., Andreon S., 2008, A&A, 490, 923

Moore B., Katz N., Lake G., Dressler A., Oemler A., 1996, Nature, 379, 613

Moran S. M., Ellis R. S., Treu T., Salim S., Rich R. M., Smith G. P., Kneib J.-P., 2006, ApJL, 641, L97

Morrissey P., et al., 2007, ApJS, 173, 682

Muzzin A., et al., 2013, ApJ, 777, 18

Nantais J. B., et al., 2016, A&A, 592, A161

O'Connell R. W., 1976, ApJ, 206, 370

Peebles P. J. E., 1982, ApJL, 263, L1

Peng C. Y., Ho L. C., Impey C. D., Rix H.-W., 2002, AJ, 124, 266

Peng C. Y., Ho L. C., Impey C. D., Rix H.-W., 2010a, AJ, 139, 2097

Peng Y.-j., et al., 2010b, ApJ, 721, 193

Perlmutter S., et al., 1999, ApJ, 517, 565

Planck Collaboration et al., 2020, A&A, 641, A6

Poggianti B. M., Smail I., Dressler A., Couch W. J., Barger A. J., Butcher H., Ellis R. S., Oemler Augustus J., 1999, ApJ, 518, 576

Poggianti B. M., Bridges T. J., Komiyama Y., Yagi M., Carter D., Mobasher B., Okamura S., Kashikawa N., 2004, ApJ, 601, 197

Poggianti B. M., et al., 2017, ApJ, 844, 48

Postma J. E., Leahy D., 2017, PASP, 129, 115002

Pozzetti L., et al., 2003, A&A, 402, 837

Press W. H., Schechter P., 1974, ApJ, 187, 425

Quilis V., Moore B., Bower R., 2000, Science, 288, 1617

Quilis V., Bower R. G., Balogh M. L., 2001, MNRAS, 328, 1091

Reed D., Gardner J., Quinn T., Stadel J., Fardal M., Lake G., Governato F., 2003, MNRAS, 346, 565

Reed D. S., Bower R., Frenk C. S., Jenkins A., Theuns T., 2007, MNRAS, 374, 2

Reiprich T. H., Böhringer H., 2002, ApJ, 567, 716

Riess A. G., et al., 1998, AJ, 116, 1009

Roberts I. D., Parker L. C., 2020, MNRAS, 495, 554

Roberts I. D., et al., 2022a, MNRAS, 509, 1342

Roberts I. D., van Weeren R. J., Timmerman R., Botteon A., Gendron-Marsolais M., Ignesti A., Rottgering H. J. A., 2022b, A&A, 658, A44

Rodriguez-Gomez V., et al., 2019, MNRAS, 483, 4140

Sazonova E., et al., 2020a, ApJ, 899, 85

Sazonova E., et al., 2020b, ApJ, 899, 85

Sérsic J. L., 1963, Boletin de la Asociacion Argentina de Astronomia La Plata Argentina, 6, 41

Sheth R. K., Mo H. J., Tormen G., 2001, MNRAS, 323, 1

Simard L., 1998, in Albrecht R., Hook R. N., Bushouse H. A., eds, Astronomical Society of the Pacific Conference Series Vol. 145, Astronomical Data Analysis Software and Systems VII. p. 108

Simard L., et al., 2002, ApJS, 142, 1

Simard L., Mendel J. T., Patton D. R., Ellison S. L., McConnachie A. W., 2011, ApJS, 196, 11

Smith R. J., et al., 2010, MNRAS, 408, 1417

Somerville R. S., 2002, ApJL, 572, L23

Somerville R. S., Davé R., 2015, ARA&A, 53, 51

Springel V., Di Matteo T., Hernquist L., 2005a, MNRAS, 361, 776

Springel V., et al., 2005b, Nature, 435, 629

Steinhauser D., Haider M., Kapferer W., Schindler S., 2012, A&A, 544, A54

Stone C. J., Arora N., Courteau S., Cuillandre J.-C., 2021, MNRAS, 508, 1870

Tandon S. N., et al., 2020, AJ, 159, 158

Tonnesen S., Bryan G. L., 2009, ApJ, 694, 789

Tornatore L., Borgani S., Springel V., Matteucci F., Menci N., Murante G., 2003, MNRAS, 342, 1025

Veilleux S., Cecil G., Bland-Hawthorn J., 2005, ARA&A, 43, 769

Vollmer B., Cayatte V., Balkowski C., Duschl W. J., 2001, ApJ, 561, 708

Vulcani B., et al., 2018, ApJL, 866, L25

Watson W. A., Iliev I. T., D'Aloisio A., Knebe A., Shapiro P. R., Yepes G., 2013, MNRAS, 433, 1230

Weinmann S. M., van den Bosch F. C., Yang X., Mo H. J., 2006, MNRAS, 366, 2

Weinmann S. M., Pasquali A., Oppenheimer B. D., Finlator K., Mendel J. T., Crain R. A., Macciò A. V., 2012, MNRAS, 426, 2797

Wetzel A. R., Tinker J. L., Conroy C., 2012, MNRAS, 424, 232

White S. D. M., Frenk C. S., 1991, ApJ, 379, 52

Wolf C., Gray M. E., Meisenheimer K., 2005, A&A, 443, 435

Wolf C., et al., 2009, MNRAS, 393, 1302

Yagi M., Komiyama Y., Yoshida M., Furusawa H., Kashikawa N., Koyama Y., Okamura S., 2007, ApJ, 660, 1209

Yagi M., et al., 2010, AJ, 140, 1814

Yang H. Y. K., Reynolds C. S., 2016, ApJ, 829, 90

York D. G., et al., 2000, AJ, 120, 1579

Zwicky F., 1933, Helvetica Physica Acta, 6, 110

de Vaucouleurs G., 1948, Annales d'Astrophysique, 11, 247

van den Bergh S., 1976, ApJ, 206, 883

van den Bosch F. C., Aquino D., Yang X., Mo H. J., Pasquali A., McIntosh D. H., Weinmann S. M., Kang X., 2008, MNRAS, 387, 79

APPENDICES

Appendix A

GALFIT S/N and Input Testing

We discuss various tests run using GALFIT and MEGAMORPH software on both simulated UV galaxy images and our actual UVIT data to determine the most effective inputs for fitting Sérsic profiles.

When run as a standalone fitting code, GALFIT has several user input options to help the code produce a good Sérsic fit to the galaxy image. First off, GALFIT allows the user the option to input a weightmap (each pixel value is 1σ uncertainty), or allow GALFIT to calculate the weightmap internally given the detector gain. The gain is a value that amplifies the number of photoelectrons displaced from a pixel on a detector to a digital number value. In the case of UVIT, our science images have pixel values already in the correct units for noise determination, so we set the gain to 1. One issue we have in creating our own weightmap is handling pixels with 0 counts, which from a simple Poisson uncertainty determination would have 0 uncertainty. We find that the GALFIT internal weightmap determination does a better job at producing a smooth weightmap.

In order for GALFIT to produce its internal weightmap, it needs to either measure the background and background uncertainty or be given this value by the user. We have tested both and found minimal differences in the accuracy of the final fit. Additionally, GALFIT can fit the background simultaneously with the galaxy, or the user can specify the background object be held fixed at some pre-determined value. Since the UV background is very low and not well represented by Gaussian statistics, we have chosen to fix the background during the GALFIT fitting run. We did, however, sometimes find marginally better fits when we let GALFIT fit the background. The caveat is that the background object itself came out with a less accurate value based on the known value. We show an example in Figure A.1 for an $n = 4$ galaxy, since we found these differences to only be
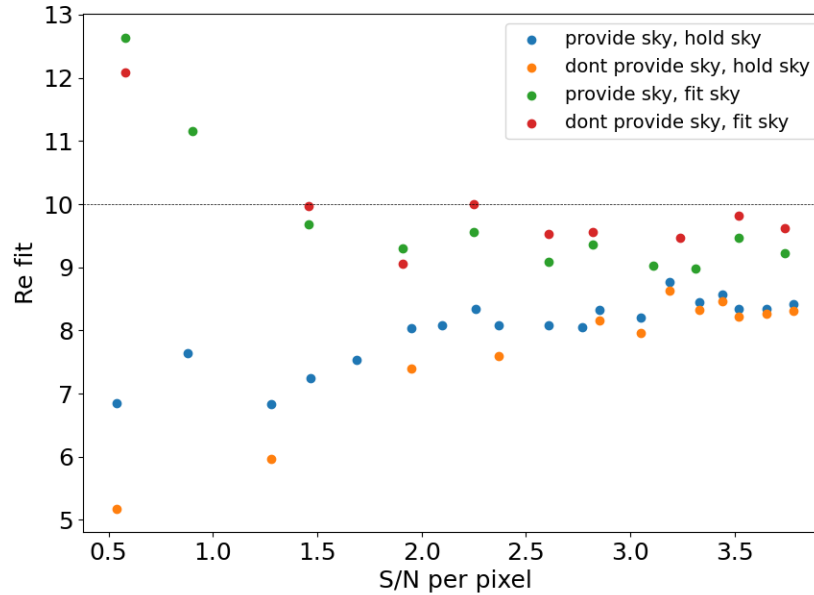
considerable with higher Sérsic indices.

Figure A.1: Four tests of GALFIT performed on a simulated UV galaxy. Red: allow GALFIT to measure background for weightmap and then fit background with galaxy. Green: provide background value for weightmap, but allow to be fit with galaxy. Orange: Let GALFIT measure background for weightmap but hold known background value fixed during fitting. Blue: provide background level for weightmap and hold fixed during fitting.

While the results from Fig. A.1 hint that for this simulated object, allowing GALFIT to fit the background may give marginally better fit, simulating many more realizations of this test would likely result in more scatter. Nonetheless, we decided to run MEGAMORPH with GALFIT background fitting both turned on and off to see if that factor made a difference in the results of our actual UVIT data. We show the results in Figure A.2, with the black data points being fit background and the red being fixed background. We see almost no change in the results at higher S/N, and a small change in the scatter at lower S/N.
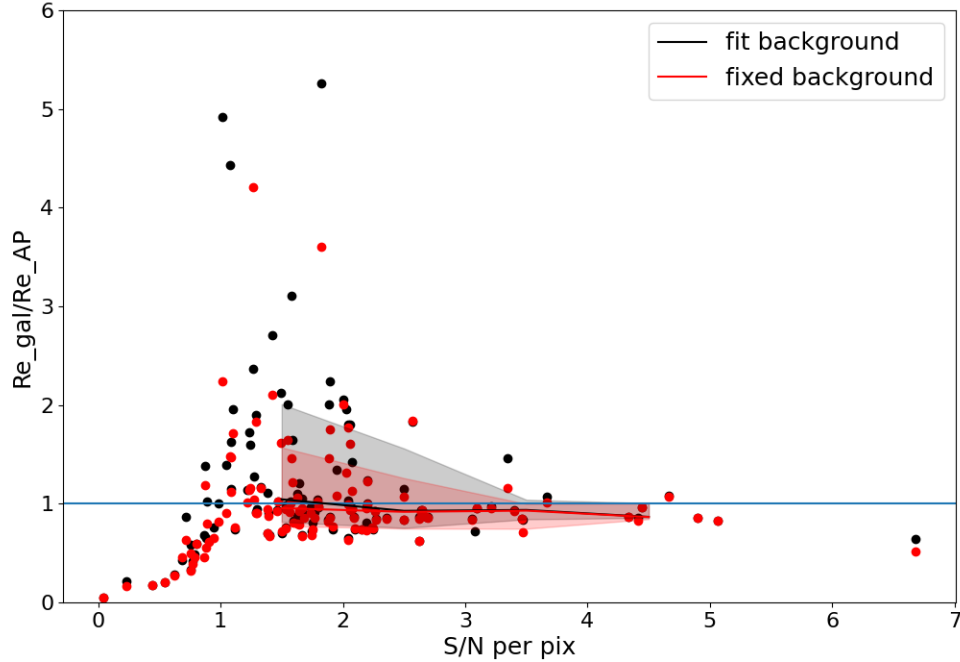
Figure A.2: Ratio of GALFIT fits to AUTOPROF/growth curve method fits for two runs of MEGAMORPH as a function of S/N per pixel. The data points in black are where GALFIT was allowed to fit the background, while the red is where the previously measured background was held fit through the GALFIT run. The solid lines show the median values in S/N bins, and the shades regions show the 1σ intervals.

This lead us to consider the possibility that our GALFIT fits were particularly poor due to the use of the MEGAMORPH wrapper. Using that wrapper, there was less user control over the input into GALFIT itself without significant modifications to the code. As such, we wrote our own wrapper to cut postage stamps and assign the desired user inputs to GALFIT to test out the difference between letting GALFIT fit the background versus holding it fixed. We show these results in Figure A.3, comparing our GALFIT wrapper to MEGAMORPH. Note that, beyond a S/N per pixel of 2, we see almost no difference between holding the background fixed (top panel of Fig. A.3) and letting GALFIT fit it (bottom panel). We do see a change in the scatter below S/N per pixel of 2, but arguably the results are better for the fixed background plot (top panel of Fig. A.3), contrary to the result of Fig. A.1. Ultimately we chose to use the MEGAMORPH results with fixed

background in the plots shown in this thesis, but it is clear our results would not change if we chose to use our own wrapper instead for the galaxies with higher S/N. We also tried different sized segmentation maps in our GALFIT wrapper to make the process more similar to STATMORPH. However we found that any size segmentation map produced much worse results (figures not shown).
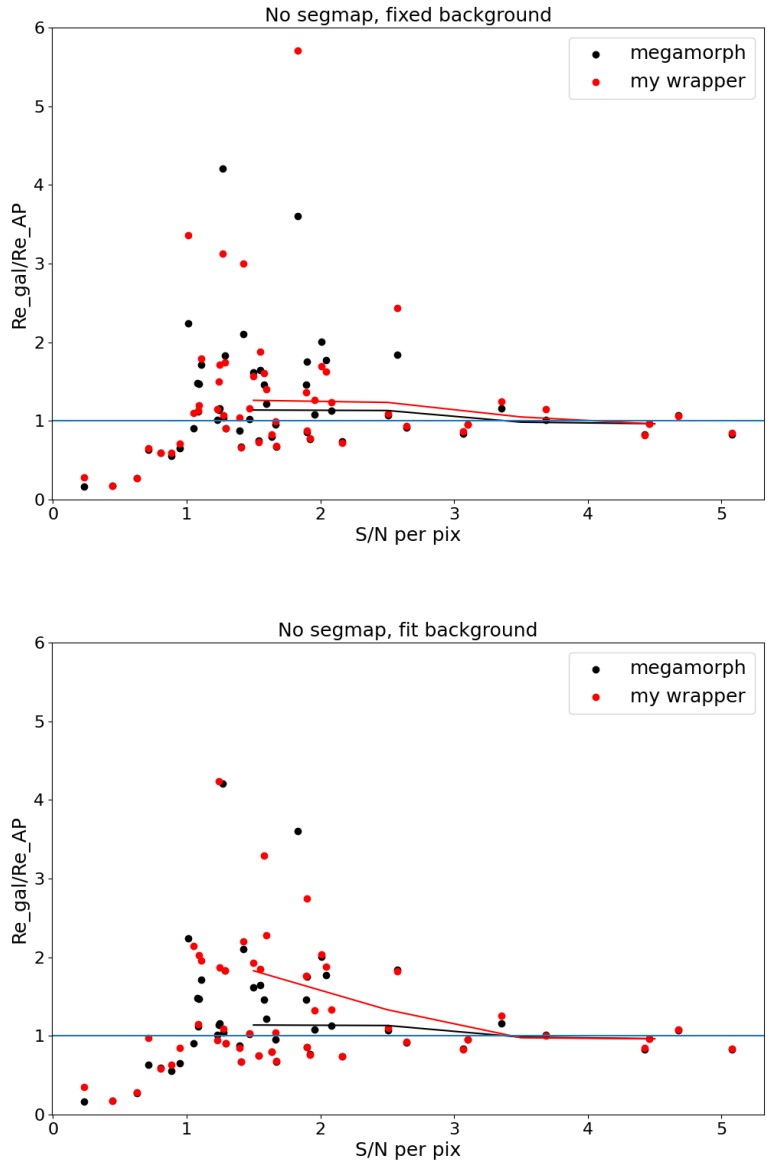
Figure A.3: Ratio of GALFIT fits to AUTOPROF/growth curve method fits for MEGAMORPH compared to our own wrapper for GALFIT as a function of S/N per pixel. The data points in black are the MEGAMORPH run with fixed background in both the top and bottom plots. In the top plot, we fix the background in GALFIT for our own wrapper as well (red), and in the bottom we let GALFIT fit the background.

Appendix B

Additional Figures
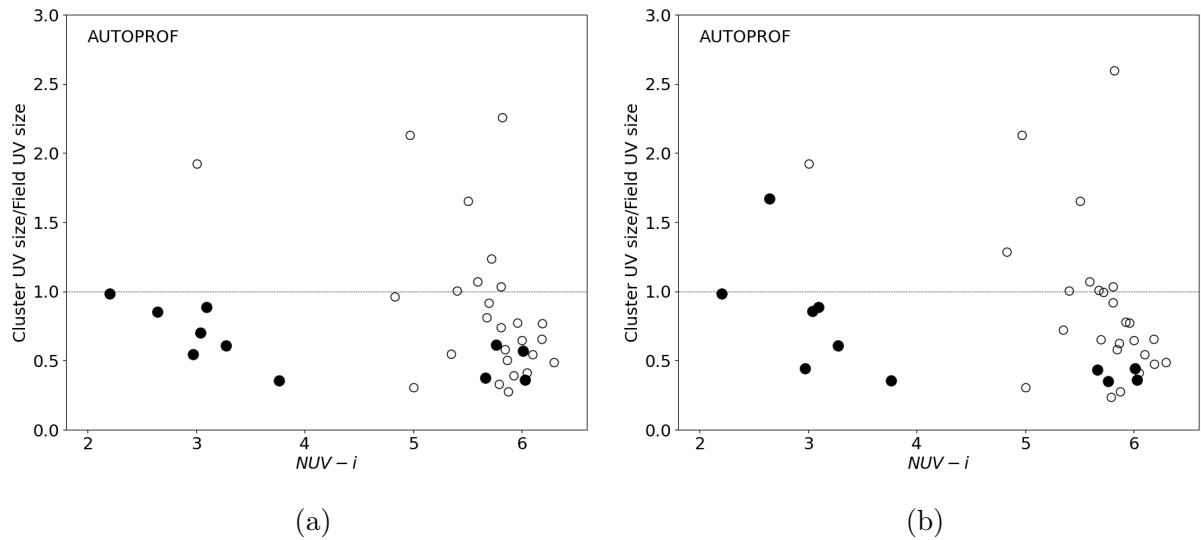
Figure B.1: Ratios of Coma galaxy UV sizes (r_e) to the sizes of their field counterparts as a function of $NUV - i$ colour. Results in (a) include the optical size matching criterion, while results in (b) do not. Data point sizes are the same as in Fig. 4.5
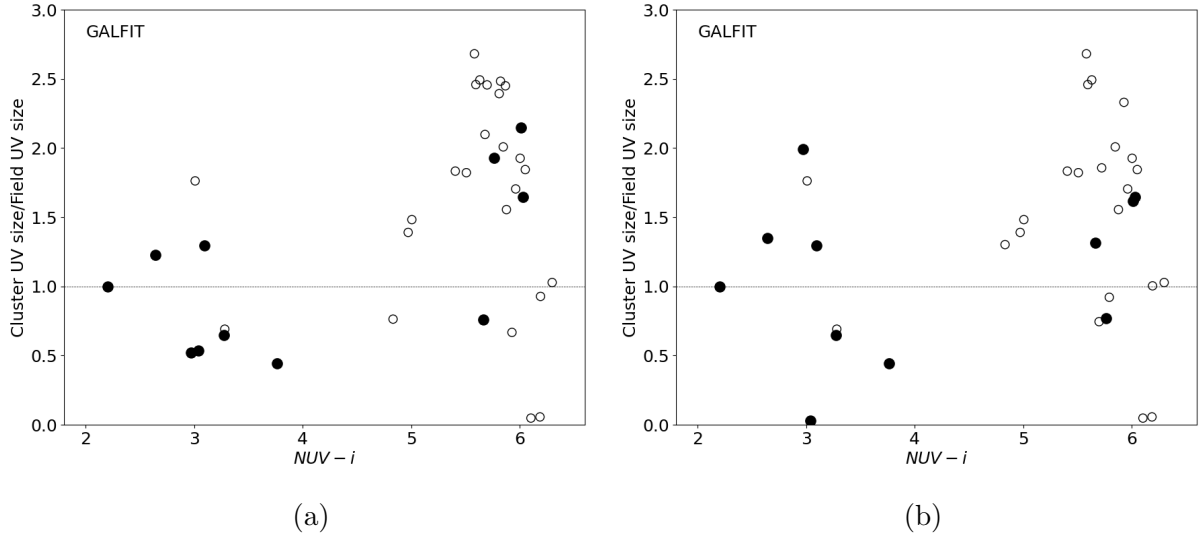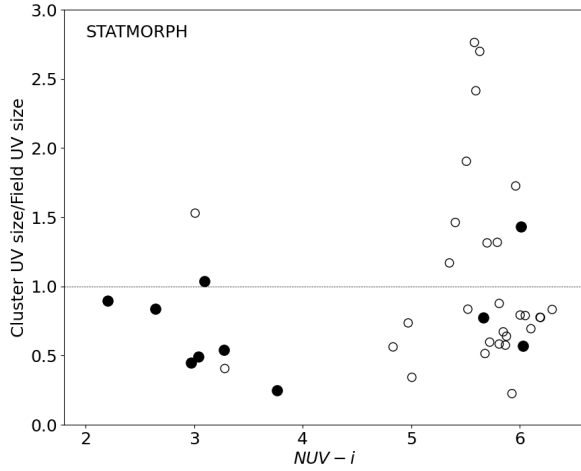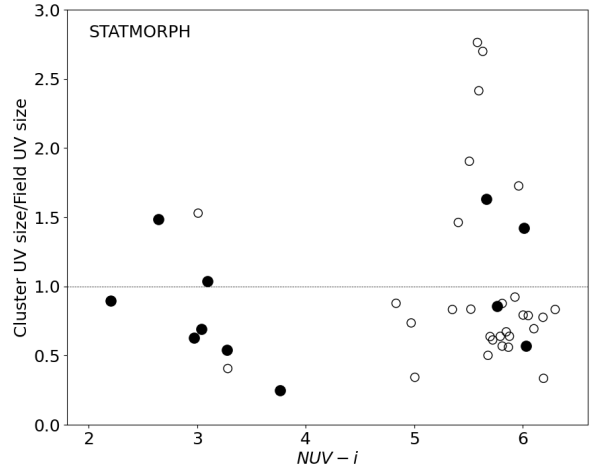
Figure B.2: Same as Figure B.1 but using GALFIT for both cluster and field r_e fits instead of AUTOPROF/growth curve fits

(a)

(b)

Figure B.3: Same as Figure B.1 but using STATMORPH for both cluster and field r_e fits instead of AUTOPROF/growth curve fits
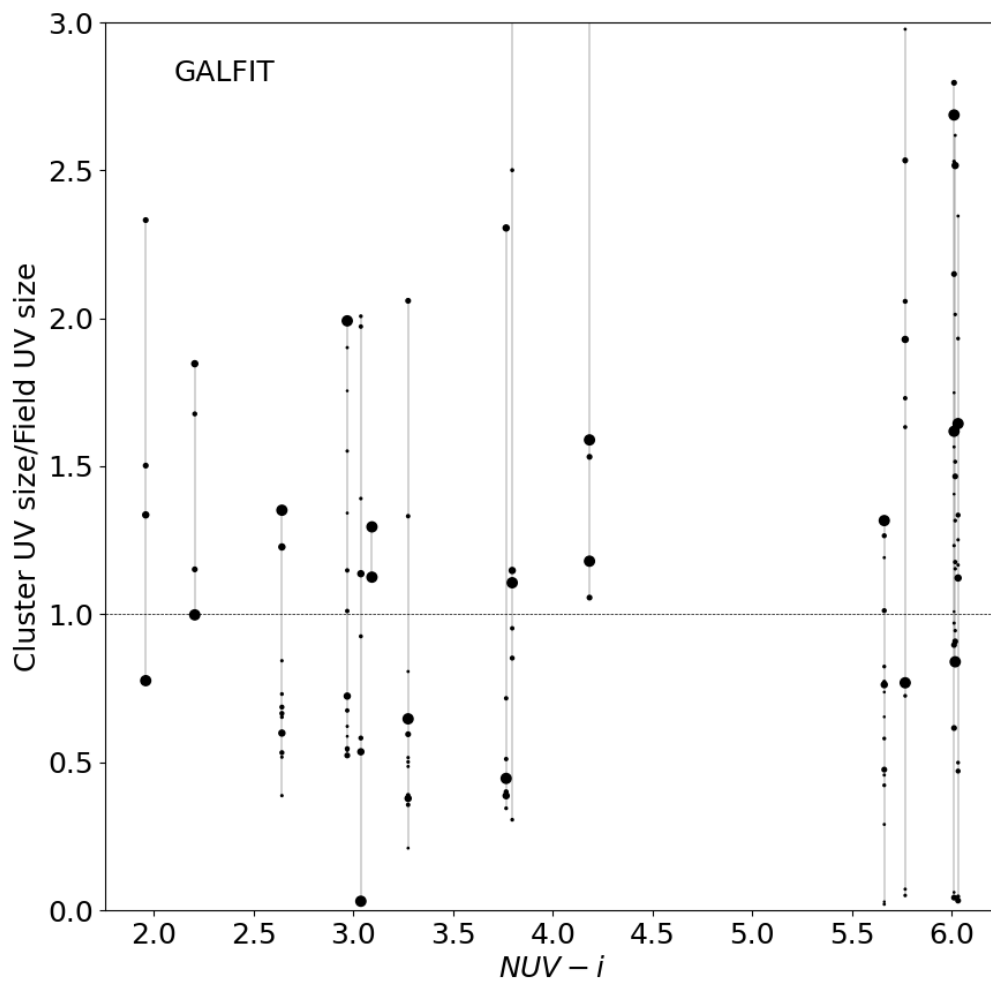
Figure B.4: Same as Figure 4.4 but using GALFIT for both cluster and field r_e fits instead of AUTOPROF/growth curve fits
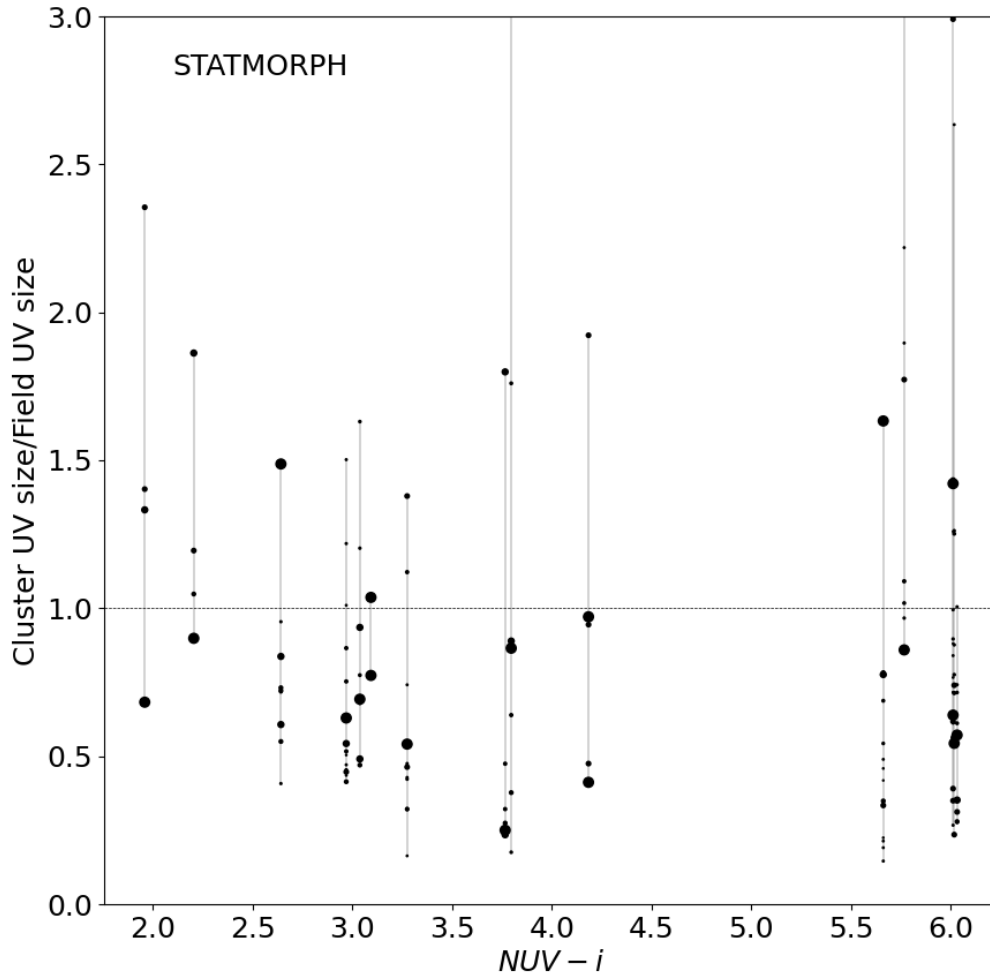
Figure B.5: Same as Figure 4.4 but using STATMORPH for both cluster and field r_e fits instead of AUTOPROF/growth curve fits